1 **Impacts of Cloud Microphysics Parameterizations on Simulated Aerosol-Cloud-Interactions**

2 **for Deep Convective Clouds over Houston**

3

4 Yuwei Zhang[1, 2], Jiwen Fan[2, *], Zhanqing Li[1], Daniel Rosenfeld[3]

5

6 [1]Department of Atmospheric and Oceanic Science, University of Maryland, College Park, MD,

7 USA

8 [2]Atmospheric Sciences and Global Change Division, Pacific Northwest National Laboratory,

9 Richland, WA, USA

10 [3] Institute of Earth Sciences, The Hebrew University of Jerusalem, Jerusalem, Israel

11 * *Correspondence to*: Jiwen Fan (jiwen.fan@pnnl.gov)

12

13

Abstract

Aerosol-cloud interactions remain largely uncertain in predicting their impacts on weather and climate. Cloud microphysics parameterization is one of the factors leading to the large uncertainty. Here we investigate the impacts of anthropogenic aerosols on the convective intensity and precipitation of a thunderstorm occurring on 19 June 2013 over Houston with the Chemistry version of Weather Research and Forecast model (WRF-Chem) using the Morrison two-moment bulk scheme and spectral-bin microphysics (SBM) scheme. We find that the SBM predicts a deep convective cloud agreeing better with observations in terms of reflectivity and precipitation compared with the Morrison bulk scheme that has been used in many weather and climate models. With the SBM scheme, we see a significant invigoration effect on convective intensity and precipitation by anthropogenic aerosols mainly through enhanced condensation latent heating (i.e., the warm-phase invigoration). Whereas such an effect is absent with the Morrison two-moment bulk microphysics, mainly because the saturation adjustment approach for droplet condensation and evaporation calculation removes the dependence of condensation on droplet properties and limits the ice processes by a more efficient conversion of droplets into raindrops, which leads to less cloud droplets being transported to the altitudes above the freezing level.

1 Introduction

Deep convective clouds (DCCs) produce copious precipitation and play important roles in the hydrological and energy cycle as well as regional and global circulation (e.g., Arakawa, 2004; Houze, 2014). DCCs and associated precipitation are determined by water vapor, vertical motion of air, and cloud microphysics that could be affected by aerosols through aerosol-radiative interactions (ARI) or aerosol-cloud interactions (ACI) or both. The cloud-mediated aerosol effects are recognized by the Intergovernmental Panel on Climate Change (IPCC) as one of the key sources of uncertainty in our knowledge of Earth's energy budget and anthropogenic climate forcing (e.g., Arakawa, 2004; Andreae et al., 2005; Haywood and Boucher, 2000; Lohmann and Feichter, 2005).

Precipitation, latent heat, and cloud radiative forcing associated with DCCs are strongly associated with cloud microphysical processes, which can be modulated by aerosols through serving as cloud condensation nuclei (CCN) and ice nuclei (IN). For aerosol-DCC interactions, a well-known theory is that increasing aerosol concentrations can suppress warm rain as a result of increased droplet number but reduced droplet size. This allows more cloud droplets to be lifted to altitudes above the freezing level, inducing stronger ice microphysical processes (e.g., droplet freezing, riming, and deposition) which release larger latent heating, thereby invigorating convective updrafts (referred to as "cold-phase invigoration,"; Khain et al. 2005; Rosenfeld et al., 2008). It is significant in the situations of warm-cloud bases (> 15°C; Fan et al., 2012b; Li et al., 2011; Rosenfeld et al., 2014; Tao and Li, 2016) and weak wind shear (Fan et al., 2009, 2012b, 2013; Li et al., 2008; Lebo et al., 2012). Grabowski and Morrison (2016; 2020) rejected this invigoration concept by arguing that the increase in the buoyancy by freezing is completely offset by the buoyancy for carrying the extra cloud water across the freezing level. However, Rosenfeld

54 et al. (2008) showed that the buoyancy restores and increases after the precipitation of the ice

55 hydrometeors that form upon freezing of the high supercooled liquid water content into large

56 graupel and hail.

57 Another theory is that increasing aerosols enhances droplet nucleation particularly secondary

58 nucleation after warm rain initiates, which promotes condensation because of larger integrated

59 droplet surface area associated with a higher number of small droplets (Fan et al., 2007, 2013,

60 2018; Koren at al., 2014; Lebo, 2018; Sheffield et al., 2015; Chen et al., 2020). This so-called

61 "warm-phase invigoration", which is manifested in a warm, humid, and clean environment under

62 which the addition of a large number of ultrafine aerosol particles from urban pollution leads to

63 stronger invigoration than the "cold-phase invigoration" (Fan et al., 2018). Grabowski and

64 Morrison (2020) proposed a different interpretation of the warm-phase invigoration from the

65 literature listed above. They argued that condensation rates only depend on updraft velocity with

66 the quasi-steady assumption (i.e., the true supersaturation is approximated with the equilibrium

67 supersaturation), therefore they interpreted that it is the lower equilibrium supersaturation in

68 polluted conditions that lead to a larger buoyancy, thus enhanced updraft speeds, and condensation.

69 Several studies showed that the quasi-steady assumption is invalidated in the conditions of low

70 droplet concentrations (Politovich and Cooper, 1988; Korolev and Mazin, 2003) or acceleration of

71 vertical velocity (Pinsky et al., 2013).

72 Many factors can affect whether aerosols invigorate or suppress convective intensity through

73 ACI, such as environmental wind shear (Fan et al., 2009; Lebo et al., 2012), relative humidity (Fan

74 et al., 2007; Khain et al., 2008), and Convective Available Potential Energy (Lebo et al., 2012;

75 Morrison, 2012; Storer et al., 2010). Meteorological buffering effects were also found for aerosol

76 effects on convective clouds over a large region and long-time (over a few days and weeks)

77 simulations (Stevens and Feingold, 2009; van den Heever et al., 2011). Dagan et al. (2018) showed

78 that the lifetimes of cloud systems are mostly much shorter than that and rarely reach this buffering

79 state. For DCCs with complicated dynamics, thermodynamics, and microphysics, aerosol impacts

80 are extremely complex and still remain poorly known. Confidently isolating and quantifying an

81 aerosol deep convective invigoration effect from observations requires very long-term

82 measurements: data of 10 years are still not enough over the Southern Great Plains due to the large

83 variability of meteorological conditions (Varble, 2018).

84   Modeling of ACI is quite dependent on cloud microphysics parameterization schemes (e.g.,

85 Fan et al., 2012a; Khain and Lynn, 2009; Khain et al., 2009, 2015; Lebo and Seinfeld, 2011; Lee

86 et al., 2018; Loftus and Cotton, 2014; Wang et al., 2013). Two-moment bulk and bin schemes have

87 been widely used in ACI studies (e.g., Chen et al., 2011; Fan et al., 2013; Khain et al., 2010). In

88 two-moment bulk schemes, hydrometeor size distributions are diagnosed from the predicted

89 number and mass with an assumed spectral shape (e.g., gamma function). The saturation

90 adjustment approach is often used for calculating condensation and evaporation, meaning

91 supersaturation and undersaturation with respect to water are removed in cloud within a timestep.

92 Some bulk schemes take the explicit supersaturation approach to allow supersaturation to evolve

93 (e.g., Morrison and Grabowski, 2007; 2008). In bin schemes, the size distributions of hydrometeors

94 are discretized by a number of size bins and predicted, which represents some aerosol-cloud

95 interaction processes more physically compared with bulk schemes (Fan et al., 2016; Khain et al.,

96 2015). Supersaturation is generally predicted in bin schemes.

97   Many studies have shown that bulk schemes are limited in representing certain important

98 microphysical processes such as aerosol activation, condensation, deposition, sedimentation, and

99 rain evaporation (Ekman et al., 2011; Khain et al., 2009; Lee et al. 2018; Li et al., 2009; Milbrandt

100   and Yau, 2005; Morrison, 2012; Wang et al., 2013). Though bin cloud microphysics can provide

101   a more rigorous numerical solution and a more robust cloud microphysics representation than

102   typical bulk microphysics, it is often applied in simulations for process understanding but rarely

103   in operational applications due to the expensive computation cost. For not introducing further

104   computation cost, bins schemes are also often run with a prescribed aerosol spectrum assuming a

105   fixed composition and a simple aerosol budget treatment without coupling with chemistry/aerosol

106   calculations. As a result, many aerosol life cycle processes such as aerosol nucleation, growth,

107   aqueous chemistry, aerosol resuspension, and below-cloud wet removal are missing or crudely

108   parameterized. Therefore, it is difficult to simulate the spatial and temporal variabilities of aerosol

109   chemical composition and size distribution. In Gao et al. (2016), we have coupled a spectral-bin

110   microphysics scheme (SBM; Fan et al., 2012a; Khain et al., 2004) with the Chemistry version of

111   Weather Research and Forecast model (WRF-Chem; Grell et al., 2005; Skamarock et al., 2008),

112   called WRF-Chem-SBM, to address above-mentioned limitations. In this new model, the SBM

113   was coupled with the Model for Simulating Aerosol Interactions and Chemistry (MOSAIC; Fast

114   et al., 2006; Zaveri et al., 2008). The newly coupled system was initially evaluated for warm

115   marine stratocumulus clouds and showed a much-improved simulation of cloud droplet number

116   concentration and liquid water content compared with the default Morrison two-moment bulk

117   scheme (Gao et al., 2016).

118   The Houston area in summer, where isolated convective clouds with very warm cloud-bases

119   often occurred in the afternoon (Yuan et al., 2008), offers (a) a combination of polluted aerosols

120   from the urban and industrial area of Houston with significantly low background aerosol

121   concentrations surrounding Houston, (b) aerosol sources that are not correlated with meteorology,

122   and (c) weak synoptic forcing along with strong local triggering in the form of land-sea contrasts

123 and sea breeze fronts. This combination allows the manifestation of potentially large aerosol

124 effects. In this study, we choose a sea-breezed induced DCC case occurring 19-20 June 2013 near

125 Houston to (1) evaluate the performances of WRF-Chem-SBM in simulating deep convective

126 clouds and (2) gain a better understanding of the differences in aerosol effects predicted by SBM

127 and the Morrison two-moment bulk scheme as well as the major factors/processes responsible for

128 the differences. Considering that the convective clouds over the Houston area are mainly impacted

129 by the aerosols produced from anthropogenic activities, we focus on the anthropogenic aerosol

130 effect in this study. The simulated storm case is the same as the case for the Aerosol-Cloud-

131 Precipitation-Cloud (ACPC) Model Intercomparison Project (Rosenfeld et al., 2014;

132 www.acpcinitiative.org).

133 **2 Case Description and Observational Data**

134   A local convective event near Houston, Texas on 19-20 June 2013 is selected for the study

135 owing to the most favorable conditions for simulating isolated convective cells. As above-

136 mentioned, the case is also selected for the ACPC Model Intercomparison Project

137 (www.acpcinitiative.org). The isolated relatively weak convective clouds started from the late

138 morning because of a trailing front. With increased solar radiation in the early afternoon and

139 strengthening of a sea breeze circulation that transports warm and humid air from the Gulf of

140 Mexico to Houston urban area, deep convective cells over Houston and Galveston bay areas

141 developed (Fig. 1). The strong convective cell observed near the Houston city was initiated around

142 2145 UTC (local time 16:45) and developed to its peak precipitation at 2217 UTC based on radar

143 observation (Fig. 1). The maximum reflectivity was more than 55 dBZ. This storm cell lasted for

144 about 1.5 hours.

145   We used the following observation data for model evaluation. Particulate matter (PM) 2.5

146   data provided by Texas Commission for Environmental Quality (TCEQ) at

147   https://www.tceq.texas.gov/agency/data/pm25.html are used to evaluate the simulated aerosols

148   near the surface. The data for evaluating cloud base heights and CCN number concentration at

149   cloud base are obtained from the Visible Infrared Imaging Radiometer Suite (VIIRS) retrievals

150   based on the method of Rosenfeld et al., (2016). The 2-m temperature and 10-m winds are from

151   the North American Land Data Assimilation System (NLDAS) with 0.125-deg resolution at

152   https://climatedataguide.ucar.edu/climate-data/nldas-north-american-land-data-assimilation-

153   system. The observed radar reflectivity is used to evaluate the simulated convective system. The

154   radar reflectivity is obtained from Next-Generation Weather Radar (NEXRAD) network at

155   https://www.ncdc.noaa.gov/data-access/radar-data/nexrad-products, with a temporal frequency of

156   every ~ 5 minutes and 1 km horizontal spatial resolution.

157   **3. Model description and experiments**

158   We conducted model simulations using the version of WRF-Chem based on Gao et al.

159   (2016) coupling with the Morrison two-moment scheme (Morrison et al., 2005; Morrison et al.,

160   2009; Morrison and Milbrandt, 2011) and SBM (Khain et al., 2004; Fan et al., 2012). The version

161   of SBM employed in this study is a fast version of the Hebrew University Cloud Model (HUCM)

162   described by Khain et al. (2004) with improvements from Fan et al. (2012a) and (2017). The

163   considered hydrometer size distributions are droplets/raindrops, cloud ice/snow, and graupel. The

164   graupel version is used because it is more appropriate for simulating the convective storm over the

165   Houston area than the hail version. SBM is currently coupled with the four-sector version of

166   MOSAIC (0.039-0.156, 0.156-0.624, 0.624-2.5 and 2.5-10.0 μm). As detailed in Gao et al. (2016),

167   the aerosol processes including aerosol activation, resuspension, and in-cloud wet-removal are also

168   improved. Theoretically, both aerosol and cloud processes can be more realistically simulated

169   particularly under the conditions of complicated aerosol compositions and aerosol spatial

170   heterogeneity compared with original WRF-Chem. The dynamic core of WRF-Chem-SBM is the

171   Advanced Research WRF model that is fully compressible and non-hydrostatic with a terrain-

172   following hydrostatic pressure vertical coordinate (Skamarock et al., 2008). The grid staggering is

173   the Arakawa C-grid. The model uses the Runge-Kutta 3rd order time integration schemes, and the

174   3rd and 5th order advection schemes are selected for the vertical and horizontal directions,

175   respectively. The positive definite option is employed for advection of moist and scalar variables.

176   Two nested domains with horizontal grid spacings of 2 and 0.5 km and horizontal grid points

177   of 450×350 and 500×400 for Domain 1 and Domain 2, respectively, are used (Fig. 2a), with 51

178   vertical levels up to 50 hPa which allows about 50-100 m grid spacings below 2-km altitude and

179   ~500 m above it. The simulations for Domain 1 and Domain 2 are run separately and the Domain

180   1 simulations serve to provide the chemical and aerosol lateral boundary and initial conditions of

181   Domain 2. The chemical and aerosol lateral boundary and initial conditions for Domain 1

182   simulations were from a quasi-global WRF-Chem simulation at 1-degree grid spacing, and

183   meteorological lateral boundary and initial conditions were created from MERRA-2 at the grid

184   spacing of $0.5° \times 0.625°$ (Gelaro et al., 2017). Two simulations were run over Domain 1 with

185   anthropogenic emissions turned on and off, respectively, to provide two different aerosol scenarios

186   for the initial and boundary chemical and aerosol conditions for Domain 2 simulations: (1) a

187   polluted aerosol scenario with anthropogenic aerosols accounted which is for the real situation; (2)

188   an assumptive clean scenario without anthropogenic aerosols. Domain 2 is run with initial and

189   lateral boundary chemical and aerosols fields from Domain 1 outputs and initial and lateral

190   boundary meteorological conditions from MERRA-2. Note that we use the meteorology from

191 MERRA-2 as the initial and lateral boundary conditions for Domain 2 instead of Domain 1 outputs,

192 because we want to keep the initial and lateral boundary meteorological conditions the same for

193 all the sensitivity tests with different microphysics and aerosol setups (meteorology is different

194 between the two simulations over Domain 1).

195   The simulations in Domain 1 were initiated at 0000 UTC on 14 Jun and ended at 1200 UTC

196 20 June with about 5 days for the chemistry spin-up. The meteorological field was reinitialized

197 every 36 hours to prevent the model drifting. The dynamic time step was 6 s for Domain 1 and 3

198 s for Domain 2. The anthropogenic emission was from NEI-2011 emissions. The biogenic

199 emission came from the Model of Emissions of Gases and Aerosols from Nature (MEGAN)

200 product (Guenther et al., 2006). The biomass burning emission was from the Fire Inventory from

201 NCAR (FINN) model (Wiedinmyer et al., 2011). We used the Carbon Bond Mechanism Z

202 (CBMZ) gas-phase chemistry (Zaveri and Peters, 1999) and MOSAIC aerosol model with four

203 bins (Zaveri et al., 2008). The physics schemes other than microphysics applied in the simulation

204 are the Unified Noah land surface scheme (Chen and Dudhia, 2001), Mellor-Yamada-Janjic

205 planetary boundary layer scheme (Janjic et al., 1994), Multi-layer, Building Environment

206 Parameterization (BEP) urban physics scheme (Salamanca and Martilli, 2010), the RRTMG

207 longwave and shortwave radiation schemes (Iacono et al., 2008).

208   The main purpose of the simulations in Domain 1 is to provide initial and boundary chemical

209 and aerosol conditions for the simulations in Domain 2. To save computational cost, WRF-Chem

210 coupled with Morrison two-moment bulk microphysics scheme (Morrison et al., 2005) is used for

211 the simulations in Domain 1. Two simulations run for Domain 1 are referred to as D1_MOR_anth

212 in which the anthropogenic emissions are turned on and D1_MOR_noanth where the

213 anthropogenic emissions are turned off. Then four major experiments are carried out to simulate

214 the convective event near Houston over Domain 2 with two cloud microphysics schemes and two

215 aerosol scenarios, respectively. We refer to the simulation in which SBM is used and the

216 anthropogenic emissions are included using the initial and boundary chemicals and aerosols from

217 D1_MOR_anth, as our baseline simulation (referred to as "SBM_anth"). SBM_noanth is based on

218 SBM_anth but uses initial and boundary chemicals and aerosols from D1_MOR_noanth and turns

219 off the anthropogenic emissions, meaning that anthropogenic aerosols are not taken into account.

220 MOR_anth and MOR_noanth are the two corresponding simulations to SBM_anth and

221 SBM_noanth, respectively, using the Morrison two-moment bulk microphysics scheme. To

222 examine the contribution of the saturation adjustment approach for condensation and evaporation

223 to the simulated aerosol effects with the Morrison scheme, we further conducted two sensitivity

224 tests, based on MOR_anth and MOR_noanth, by replacing the saturation adjustment approach in

225 the Morrison scheme with the condensation and evaporation calculation based on an explicit

226 representation of supersaturation over a time step as described in Lebo et al. (2012). That is the

227 supersaturation is solved by the source and sink terms of dynamic forcing and

228 condensation/evaporation within a one-timestep. Note in both SBM and this modified Morrison

229 schemes, the supersaturation for condensation and evaporation is calculated after the advection.

230 These two simulations are referred to as MOR_SS_anth and MOR_SS_noanth, respectively. To

231 present more robust results, we carry out a small number of ensembles (three) for each case over

232 Domain 2 (we do not have computer time to do more ensemble runs). The three ensemble runs are

233 only different in the initialization time: 0000 UTC, 0600 UTC, and 1200 UTC on 19 June. All the

234 simulations end at 1200 UTC 20 June. The analysis results for Domain 2 simulations in this study

235 are based on the mean values of three ensemble runs and the ensemble spread is shown as the

236 shaded area in all profile figures.

237   We evaluate the aerosol and CCN properties simulated by D1_MOR_anth to ensure realistic

238   aerosol fields, which are used for the Domain 2 simulations with anthropogenic aerosols

239   considered. These evaluations are included in section 4.1.

240   From D1_MOR_anth, we see a very large spatial variability of aerosol number concentrations

241   (Fig. 2b). There are three regions with significantly different aerosol loadings over the domain as

242   shown by the black boxes in Fig. 2b: (a) the Houston urban area, (b) the rural area about 100 km

243   northeast to Houston, and (c) Gulf of Mexico. Aerosols over the Houston urban area are mainly

244   contributed by organic aerosols, which are highly related to industrial and ship channel emissions.

245   The rural area aerosols are mainly from sulfate and sea salt aerosol is the major contributor over

246   the Gulf of Mexico. This suggests that aerosol properties are extremely heterogenous in this region.

247   The aerosols over Houston urban area are generally about 5 and 10 times higher than the rural and

248   Gulf area, respectively (Fig. 2c). The size distributions show a three-mode distribution with the

249   largest differences from the Aitken mode (peaks at 50 nm; Fig. 2c). These ultrafine aerosol

250   particles are mainly contributed by anthropogenic activities (Fig. 2b, d). With the anthropogenic

251   emissions turned off, the simulated aerosols are much lower and have much less spatial variability

252   (Fig. 2d).

253   **4 Result**

254   **4.1 Model Evaluation**

255   We first show the evaluation of the aerosol and CCN properties simulated by

256   D1_MOR_anth, which runs over Domain 1, much larger than Domain 2. As described in Table 1,

257   there are eight PM monitoring sites from TCEQ around the Houston area. Surface PM2.5 shows

258   high concentrations at Houston and its downwind regions (Fig. 3). Though not exactly the same,

259   the values from D1_MOR_anth show a similar distribution with the observations in terms of the

260   surface PM2.5 averaged over 24 hours (the day before the convection near Houston). The hourly

261   variations of ground-level PM2.5 concentrations from both observation and D1_MOR_anth for

262   these sites in the day before the convective initiation is depicted in Fig. 4. Generally, the simulated

263   hourly pattern agrees with the observation for eight stations. D1_MOR_anth reproduces the diurnal

264   variations, especially the increasing trend from 1200 UTC to 1800 UTC 19 Jun prior to the

265   initiation of deep convective cells over Houston and Galveston bay areas.

266   The evaluation of the cloud base heights and CCN at cloud bases at the warm cloud stage

267   before transitioning to deep clouds (2000 UTC) are shown in Fig.5. Over the Houston and its

268   surrounding area (black box in Fig. 5), the simulated cloud base heights are about 1.5-2 km, in an

269   agreement with the retrieved values from VIIRS satellite, which are around 1.2-1.8 km (Fig. 5a-

270   b). The retrieved CCN concentrations at cloud bases vary significantly over the domain and this

271   spatial variability is generally captured by the model (Fig. 5c-d). For example, D1_MOR_anth

272   simulates some high CCN concentrations (400-800 cm^{-3} with some above 1000 cm^{-3}) over the

273   Houston and around the Bay area, relatively low CCN values at the rural areas (about 200-600 cm^{-}

274   ^{3}), and very low values over the Gulf of Mexico (less than 200 cm^{-3}), as shown in Fig. 5d. This is

275   consistent with the spatial variability from the retrievals (Fig. 5c). The evaluation of aerosol

276   properties before the initiation of Houston convective cells and CCN at the warm cloud stage

277   before transitioning to deep clouds provides us confidence in using the chemical and aerosol fields

278   from Domain 1 outputs to feed Domain 2 simulations.

279   Now we are evaluating near-surface temperature and winds, reflectivity and precipitation

280   simulated by SBM_anth and MOR_anth. Fig. 6 shows the comparisons in 2-m temperature and

281   10-m winds at 1800 UTC (before the convective initiation). Compared with the coarse resolution

282   NLDAS data, both SBM_anth and MOR_anth capture the general temperature pattern with a little

283   overestimation at the northeast part of the domain (mainly rural area). The modeled southerly

284   winds do not reach further north as the NLDAS data, possibly because of the feedback of the small-

285   scale features which are simulated with the high resolution to mesoscale circulations. However,

286   the simulation of temperature over Houston and sea breeze winds from the Gulf of Mexico to

287   Houston is the most important in this case. SBM_anth predicts a slightly higher temperature than

288   MOR_anth in the northern part of the Houston region (purple box in Fig. 6), which agrees with

289   NLDAS better. SBM_anth gets the similar southerly winds from the Gulf of Mexico to Houston

290   as shown in NLDAS, while the southerly winds from Gulf of Mexico become very weak or

291   disappear prior to reaching Houston in MOR_anth.

292   For the Houston convective cell that we focused (red box in Fig. 7a), SBM_anth simulates

293   it well in both location and high reflectivity value (greater than 50 dBZ) in comparison with the

294   NEXRAD observation (Fig. 7a-b). The simulated composite reflectivities (i.e., the column

295   maximum) are up to 55-60 dBZ from all three ensemble members, consistent with NEXRAD.

296   With the Morrison scheme, MOR_anth simulates several small convective cells near Houston with

297   a maximum reflectivity of 55 dBZ or less (Fig. 7c). All three ensemble members consistently show

298   smaller but more scattered convective cells with the Morrison scheme compared with SBM. The

299   contoured frequency by altitude diagram (CFAD) plots for the entire storm period show that

300   SBM_anth is in a better agreement with observation compared with MOR_anth, especially for the

301   vertical structure of the high reflectivity range (greater than 48 dBZ, black dashed lines in Fig. 8)

302   and echo top heights, which can reach up to 14-15 km (Fig. 8a-b). MOR_anth overestimates the

303   occurrence frequencies of the 35-45 dBZ range and underestimates those of the low and high

304 reflectivity ranges (less than 15 dBZ or larger than 50 dBZ) as well as the echo top heights (1-2

305 km lower than SBM_anth; Fig. 8c).

306   For the precipitation rates averaged over the study area (red box in Fig. 7), the observation

307 shows two peaks, which are captured by both SBM_anth and MOR_anth (Fig. 9a). However, the

308 timing for the first peak is about 30 and 60 min earlier in SBM_anth and MOR_anth than the

309 observation, respectively. Also, SBM_anth predicts the rain rate intensities at the two peak times

310 more consistent with the observations whereas MOR_anth underestimates the rain rate intensity at

311 the second peak time (Fig. 9a). The large precipitation rates (greater than 15 mm h^{-1}) in SBM_anth

312 has a ~1.5 times larger occurrence probability than those in MOR_anth, showing a better

313 agreement with the observation (Fig. 9b). The observed accumulated rain over the time period

314 shown in Fig. 9a is about 3.8 mm, both SBM_anth (~4.5 mm) and MOR_anth (~4.2 mm)

315 overestimate the accumulated precipitation due to the longer rain period compared with the

316 observations. Overall, the performance of SBM_anth is superior to MOR_anth in simulating the

317 location and intensity of the convective storm and associated precipitation.

318 **4.2 Simulated Aerosol Effects on Cloud and Precipitation**

319   Now we look at the effects of anthropogenic aerosols on the deep convective storm

320 simulated with SBM and Morrison microphysics schemes. Fig. 9a shows that with the SBM

321 scheme, anthropogenic aerosols remarkably increase the mean surface rain rates (by ~30%; from

322 SBM_noanth to SBM_anth), mainly because of the increased occurrence frequency (nearly

323 doubled) for relatively large rain rates (i.e., 10-15 mm h^{-1} and >15 mm h^{-1}) in Fig. 9b. With the

324 Morrison scheme, the changes in mean precipitation and the PDF from MOR_noanth to

325 MOR_anth are relatively small, showing a very limited aerosol effect on precipitation. With the

326 SBM scheme, the increase in the updraft speeds by the anthropogenic aerosols is even more notable

327   than the precipitation (Fig. 10a-b). Above 5-km altitude, the occurrence frequencies of updraft

328   speed greater than 0.4% extend to much larger values, with 36 m s^{-1} at the upper levels in

329   SBM_anth while only ~ 20 m s^{-1} in SBM_noanth. With the Morrison scheme, the changes are not

330   significant by the anthropogenic aerosols (MOR_noanth vs MOR_anth in Fig. 10c-d). From

331   MOR_noanth to MOR_anth, there is a slight increase in updraft speed at around 9-11 km altitudes

332   but a slight decrease at 6-8 km altitudes. The significant invigoration of convective intensity by

333   anthropogenic aerosols with the SBM scheme explains the much larger occurrences of relatively

334   large rain rates and overall more surface precipitation due to the anthropogenic aerosol effect (Fig.

335   9). Note Fig. 9a shows that anthropogenic aerosols lead to an earlier start of the precipitation with

336   both SBM and Morrison, which reflects the faster transition of warm rain to mixed-phase

337   precipitation. We do see the delay of warm rain by aerosols but only about 5 min (probably due to

338   the humid condition of the case), which is difficult to be shown in Fig. 9a since averaged rain rate

339   for the analysis box is ~0.02 mm hr^{-1} and the time period is very short (~10 min).

340   Now the question is why the anthropogenic aerosols enhance the convective intensity of

341   the storm with the SBM scheme while the effect is very small with the Morrison scheme. Fig. 11

342   shows the vertical profiles of mean updraft velocity, thermal buoyancy (from temperature and

343   moisture perturbation), and total latent heating rate of the top 25th percentile updrafts with a value

344   greater than 2 m s^{-1} during the deep convective cloud stage. With the SBM microphysics scheme,

345   the increased convective intensity due to the anthropogenic aerosol effect corresponds to the

346   increased thermal buoyancy which is particularly notable at upper levels (~ 20%) from

347   SBM_noanth to SBM_anth (Fig. 11a, c). The increased thermal buoyancy can be explained by

348   the increased total latent heating (Fig. 11e), which is mainly from the larger condensation latent

349   heating (Fig. 12a). From SBM_noanth to SBM_anth, the latent heating from ice-related

350   microphysical processes (including deposition, drop freezing, and riming) has a relatively smaller

351   increase than that from condensation (about half of the increase in condensation latent heating as

352   shown in Fig. 12a). As shown in Fan et al., (2018), the increase in lower-level condensation latent

353   heating has a much larger effect on intensifying updraft intensity compared with the same amount

354   of increase in high-level latent heating from ice-related microphysical processes. This suggests

355   that the convective invigoration by the anthropogenic aerosols with the SBM scheme should be

356   mainly through the "warm-phase invigoration" mechanism. Compared with the Morrison scheme,

357   the increase of total latent heating by the anthropogenic aerosols is almost doubled with the SBM

358   scheme, explaining more remarkable enhancement of thermal buoyancy and thus the convective

359   intensity (red lines vs blue lines in Fig. 11). From MOR_noanth to MOR_anth, there is a small

360   increase in both the condensation latent heating and high-level latent heating associated with ice-

361   related processes (blue lines in Fig. 12b). The major difference in the increase of latent heating by

362   the anthropogenic aerosols between SBM and Morrison microphysics schemes comes from the

363   condensation latent heating, with a ~20% increase with SBM but only ~ 8% with Morrison (Fig.

364   12). The lack of a significant increase in condensation latent heating limits the "warm-phase

365   invigoration", mainly responsible for the limited aerosol impacts on the convective intensity and

366   associated precipitation with the Morrison scheme.

367   To understand why the responses of condensation to the anthropogenic aerosols are

368   different between the SBM and Morrison schemes, we look into the process rates of drop

369   nucleation and condensation (Fig. 13). The calculations of aerosol activation and

370   condensation/evaporation in the SBM scheme are based on the Köhler theory and diffusional

371   growth equations in light of particle size and supersaturation, receptively. Whereas in the Morrison

372   scheme, the Abdul-Razzak and Ghan (2002) parameterization is used for aerosol activation and

373   the saturation adjustment method is applied for condensation and evaporation calculation. With

374   the SBM scheme, the anthropogenic aerosols increase the drop nucleation rates by a few times

375   over the profile (red lines in Fig. 13a), and the condensation rates are also drastically increased

376   (doubled between 4-6 km altitudes as shown in Fig. 13c). The enhanced condensation rate by the

377   anthropogenic aerosols is because much more aerosols are activated to form a larger number of

378   small droplets, increasing the integrated droplet surface area for condensation, as documented in

379   Fan et al., (2018). As a result, supersaturation is drastically lower in SBM_anth than SBM_noanth

380   (green lines in Fig. 13a). With the Morrison scheme, we still see a large increase in the droplet

381   nucleation rate (Fig. 13b). However, the condensation rates are barely increased (blue solid vs.

382   dashed lines in Fig. 13d). We hypothesize that the lack of response of condensation to the increased

383   aerosol activation with the Morrison scheme is mainly because of the saturation adjustment

384   calculation of the condensation and evaporation process. The approach does not allow

385   supersaturation in cloud and the calculation does not depend on supersaturation, thus removes the

386   sensitivity to the anthropogenic aerosols.

387   To verify our hypothesis and examine how much the saturation adjustment method is

388   responsible for the weak responses of condensation latent heating and convection to the added

389   anthropogenic aerosols, we conducted two additional sensitivity tests by replacing the

390   saturation adjustment approach in the Morrison scheme with the condensation and evaporation

391   calculation based on an explicit representation of supersaturation over a time step, as described in

392   Section 3. The result shows the Morrison scheme with the simple calculation of supersaturation

393   for condensational growth significantly changes the condensation rate (orange vs. blue lines in Fig.

394   13d) and a similarly large enhancement (from MOR_SS_noanth to MOR_SS_anth in Fig. 13d) is

395   seen as the SBM scheme (Fig. 13c). This leads to a larger increase in condensation latent heating

396   (orange lines in Figure 12b) compared with the original Morrison scheme, resulting in a similarly

397   large increase in thermal buoyancy by the anthropogenic aerosols as with the SBM scheme(orange

398   lines in Fig. 11d), thus a similarly large increase in the convective intensity (orange lines in Fig.

399   11b). The increase of precipitation from MOR_SS_noanth to MOR_SS_anth is also similar to that

400   with the SBM scheme (not shown). These results verify that the saturation adjustment approach

401   for parameterizing condensation and evaporation is the major reason responsible for limited

402   aerosol effects on convective intensity and precipitation with the Morrison scheme. Past studies

403   also showed the limitations of the saturation adjustment approach in simulating aerosol impacts

404   on deep convective clouds (e.g., Fan et al., 2016; Lebo et al., 2012; Lee et al., 2018; Wang et al.,

405   2013).

406   Fig. 14 and Fig. 15 show the responses of hydrometeor mass and number to anthropogenic

407   aerosol effects. With the SBM scheme, the increases in mass and number of cloud droplets,

408   raindrops, and total ice particles (ice, snow, and graupel) by the anthropogenic aerosols are very

409   significant (Fig. 14-15, left), corresponding to convective invigoration. The increase of the total

410   ice mass is particularly significant (from 3.5 to 5.5 g kg^{-1} around 10-km altitude), suggesting a

411   large effect of enhanced convective intensity on ice hydrometeors. However, with the Morrison

412   scheme, little change is seen (Fig. 14-15, right, blue lines). By replacing the saturation adjustment

413   with a simple calculation based on supersaturation for condensation and evaporation in the

414   Morrison scheme, the increases in those hydrometeor masses become as evident as those with the

415   SBM scheme (Fig. 14-15, right, orange lines).

416   Now we explain why the saturation adjustment approach leads to smaller condensational

417   heating than the explicit supersaturation approach in Morrison Scheme and why it leads to a

418   smaller sensitivity to aerosols compared with the explicit supersaturation approach. We examine

419   the time evolution of latent heating, updraft, and hydrometeor properties. At the warm cloud stage

420   at 1700 UTC, the saturation adjustment indeed produces more condensational latent heating which

421   leads to larger buoyancy and stronger updraft intensity compared to the explicit supersaturation

422   because of removing supersaturation (Fig. 16, left, blue vs. orange). By the time of 1900 UTC

423   when the clouds have developed into mixed-phase clouds, the saturation adjustment produces less

424   condensational heating and weaker convection than the explicit supersaturation approach (Fig. 16,

425   middle). The results remain similarly later at the deep cloud stage 2100 UTC (Fig. 16, right).

426   How does this change happen from 1700 to 1900 UTC? At the warm cloud stage (17:00

427   UTC), the saturation adjustment produces droplets with larger sizes (up to 100% larger for the

428   mean radius) than the explicit supersaturation because of more cloud water produced as a result of

429   zeroing-out supersaturation at each time step (droplet formation is similar between the two cases

430   as shown in Fig. 13). This results in much faster and larger warm rain, while with the explicit

431   supersaturation rain number and mass are absent at 1700 UTC as shown in Fig. 17d and 18d). As

432   a result, when evolving into the mixed-phase stage (19:00 UTC), much fewer cloud droplets are

433   transported to the levels above the freezing level (Fig. 17b and 18b). Whereas with the explicit

434   supersaturation, because of the delayed/suppressed warm rain and smaller droplets (the mean

435   radius is decreased from 8 to 6 μm at 3 km), much more cloud droplets are lifted to the higher

436   levels. Correspondingly, a few times higher total ice particle number and mass are seen compared

437   with the saturation adjustment (Fig. 17g and 18g) because more droplets above the freezing level

438   induce stronger ice processes (droplet freezing, riming, and deposition). This leads to more latent

439   heat release (Fig. 16e), which increases the buoyancy and convective intensity. With the explicit

440   supersaturation, increasing aerosols leads to a larger reduction in droplet size (up to 1 μm more in

441   the mean radius) than the saturation adjustment, therefore more enhanced ice microphysical

442   processes and the larger latent heat. Besides, the condensational heating is more enhanced by

443   aerosols with the explicit supersaturation (Fig. 16). Together, a much larger sensitivity to aerosols

444   is seen with the explicit supersaturation.

5 Conclusions and Discussion

446   We have conducted model simulations of a deep convective cloud case occurring on 19 June

447   2013 over the Houston area with WRF-Chem coupled with the SBM and Morrison microphysics

448   schemes to (1) evaluate the performance of WRF-Chem-SBM in simulating the deep convective

449   clouds, and (2) explore the differences in aerosol effects on the deep convective clouds produced

450   by the SBM and Morrison schemes and the major factors responsible for the differences.

451   We have evaluated the simulated aerosols, CCN, cloud base heights, reflectivity, and

452   precipitation. The model simulates the large spatial variability of aerosols and CCN from the Gulf

453   of Mexico, rural areas, to Houston city. On the bulk magnitudes, the model captures the surface

454   PM2.5, cloud base height, and CCN at cloud bases near the Houston reasonably well. These

455   realistically simulated aerosol fields were fed to higher resolution simulations (0.5 km) using the

456   SBM and Morrison schemes. With the SBM scheme, the model simulates a deep convective cloud

457   over Houston in a better agreement with the observed radar reflectivity and precipitation,

458   compared with using the Morrison scheme.

459   By excluding the anthropogenic aerosols in the simulations, the effects of anthropogenic

460   aerosols on the deep convective clouds and differences in aerosol effects using the two

461   microphysics schemes were examined. With the SBM scheme, anthropogenic aerosols notably

462   increase the convective intensity, enhance the peak precipitation rate over the Houston area (by ~

463   30%), and double the frequencies of relatively large rain rates (> 10 mm h^{-1}). The enhanced

464   convective intensity by anthropogenic aerosols makes the simulated storm agree better with the

465   observed, mainly attributed to the increased condensation latent heating, indicating the "warm-

466   phase invigoration". In contrast, with the Morrison scheme, there is no significant anthropogenic

467   aerosol effect on the convective intensity and precipitation.

468   Sensitivity tests by replacing the saturation adjustment with the condensation and evaporation

469   calculation based on an explicit supersaturation approach show weaker warm clouds with smaller

470   cloud droplet sizes because of smaller condensational growth than the saturation adjustment which

471   eliminates all supersaturation. This leads to less efficient conversion of cloud droplet to rain and

472   allows more cloud droplets to be transported to altitudes above the freezing level at the mixed-

473   phase and deep cloud stages, resulting in stronger ice microphysical processes (freezing, riming,

474   and deposition), therefore larger latent heat release, invigorating convective updrafts. Lebo et al.

475   (2012) showed a similar feature that the saturation adjustment has larger total condensate mass at

476   the beginning but less at the later stage compared to the explicit supersaturation approach,

477   particularly in total ice mass. Grabowski and Morrison (2017) also showed that the saturation

478   adjustment affected ice processes by producing larger ice particles with larger falling velocities

479   compared with the explicit supersaturation approach, leading to the reduction of anvil clouds. The

480   increased condensation is significant for the enhanced warm clouds when saturation adjustment is

481   used. This is different from the points of Grabowski and Jarecka (2015) that the cloud edge

482   evaporation effect is more important for the nonprecipitating shallow clouds.

483   It is also notable that the adjusted Morrison scheme by replacing saturation adjustment with

484   explicit supersaturation for condensation and evaporation show the similar aerosol effects on

485   condensation, convective intensity, hydrometeor mass mixing ratios, and precipitation as with the

486   SBM scheme. Therefore, the saturation adjustment method for the condensation and evaporation

487   calculation is mainly responsible for the limited aerosol effects with the Morrison scheme. This is

488   because the saturation adjustment method does not allow for the "warm-phase invigoration",

489   which is different from Lebo et al. (2012) showing that the saturation adjustment artificially

490   enhanced condensation latent heating at low levels and limited the potential for aerosols to

491   invigorate convection through the "cold-phase invigoration" mechanism in their idealized

492   simulations of a supercell storm with the thermal bubble initiation. In this study of the

493   thunderstorm with WRF real-case simulations for both chemistry/aerosols and clouds, the

494   saturation adjustment method actually leads to a smaller condensation latent heating than the

495   explicit calculation with supersaturation (solid bold blue vs. solid bold orange line in Fig. 12b).

496   Thus, when the computational resource is not sufficient or in other situations such as the

497   application of SBM is not available, the Morrison scheme modified with the condensation and

498   evaporation calculation based on a simple representation of supersaturation can be applied to study

499   aerosol effects on convective clouds, especially for warm and humid cloud cases in which the

500   response of condensation to aerosols is particularly important.

501   Following Fan et al., (2018), which showed that the "warm-phase invigoration" mechanism

502   was manifested by ultrafine aerosol particles in the Amazon warm and humid environment with

503   extremely low background aerosol particles. Here we showed that in summer anthropogenic

504   aerosols over the Houston area may also enhance the thunderstorm intensity and precipitation

505   through the same mechanism by secondary nucleation of numerous ultrafine aerosol particles from

506   the anthropogenic sources. But the magnitude of the effect is not as substantial as in the Amazon

507   environment. Possible reasons include that background aerosols are much higher over the Houston

508   area and air is not as humid as Amazon.

519

520

521 **Reference**

522 Abdul-Razzak, H., and Ghan, S. J.: A parameterization of aerosol activation - 3. Sectional

523   representation, J Geophys Res-Atmos, 107, 4026, doi: 10.1029/2001jd000483, 2002.

524 Andreae, M. O., Jones, C. D., and Cox, P. M.: Strong present-day aerosol cooling implies a hot

525   future, Nature, 435, 1187-1190, doi: 10.1038/nature03671, 2005.

526 Arakawa, A.: The cumulus parameterization problem: Past, present, and future, J Climate, 17,

527   2493-2525, doi: 10.1175/1520-0442(2004)017<2493:Ratcpp>2.0.Co;2, 2004.

528 Chen, F., and Dudhia, J.: Coupling an advanced land surface-hydrology model with the Penn State-

529   NCAR MM5 modeling system. Part I: Model implementation and sensitivity, Mon

530   Weather Rev, 129, 569-585, doi: 10.1175/1520-0493(2001)129<0569:Caalsh>2.0.Co;2,

531   2001.

532 Chen Q., J. Fan, Y. Yin, and B. Han: Aerosol impacts on mesoscale convective systems forming

533   under different vertical wind shear conditions. Journal of Geophysical Research:

534   Atmospheres, 125, e2018JD030027, 2020.

535 Chen, Y. C., Xue, L., Lebo, Z. J., Wang, H., Rasmussen, R. M., and Seinfeld, J. H.: A

536   comprehensive numerical study of aerosol-cloud-precipitation interactions in marine

537   stratocumulus, Atmos Chem Phys, 11, 9749-9769, doi: 10.5194/acp-11-9749-2011, 2011.

538 Dagan, G., Koren, I., Altaratz, O. and Lehahn, Y.: Shallow convective cloud field lifetime as a key

539   factor for evaluating aerosol effects. iScience, 10, 192–202, 2018.

540 Ekman, A. M. L., Engstrom, A., and Soderberg, A.: Impact of Two-Way Aerosol-Cloud

541   Interaction and Changes in Aerosol Size Distribution on Simulated Aerosol-Induced Deep

542   Convective Cloud Sensitivity, J Atmos Sci, 68, 685-698, doi: 10.1175/2010jas3651.1,

543   2011.

Fan, J. W., Zhang, R. Y., Li, G. H., and Tao, W. K.: Effects of aerosols and relative humidity on cumulus clouds, J Geophys Res-Atmos, 112, D14204, doi: 10.1029/2006jd008136, 2007.

Fan, J. W., Yuan, T. L., Comstock, J. M., Ghan, S., Khain, A., Leung, L. R., Li, Z. Q., Martins, V. J., and Ovchinnikov, M.: Dominant role by vertical wind shear in regulating aerosol effects on deep convective clouds, J Geophys Res-Atmos, 114, D22206, doi: 10.1029/2009jd012352, 2009.

Fan, J. W., Leung, L. R., Li, Z. Q., Morrison, H., Chen, H. B., Zhou, Y. Q., Qian, Y., and Wang, Y.: Aerosol impacts on clouds and precipitation in eastern China: Results from bin and bulk microphysics, J Geophys Res-Atmos, 117, D00k36, doi: 10.1029/2011jd016537, 2012a.

Fan, J. W., Rosenfeld, D., Ding, Y. N., Leung, L. R., and Li, Z. Q.: Potential aerosol indirect effects on atmospheric circulation and radiative forcing through deep convection, Geophys Res Lett, 39, L09806, doi: 10.1029/2012gl051851, 2012b.

Fan, J. W., Leung, L. R., Rosenfeld, D., Chen, Q., Li, Z. Q., Zhang, J. Q., and Yan, H. R.: Microphysical effects determine macrophysical response for aerosol impacts on deep convective clouds, P Natl Acad Sci USA, 110, E4581-E4590, doi: 10.1073/pnas.1316830110, 2013.

Fan, J. W., Wang, Y., Rosenfeld, D., and Liu, X. H.: Review of Aerosol-Cloud Interactions: Mechanisms, Significance, and Challenges, J Atmos Sci, 73, 4221-4252, doi: 10.1175/Jas-D-16-0037.1, 2016.

Fan, J. W., Han, B., Varble, A., Morrison, H., North, K., Kollias, P., Chen, B. J., Dong, X. Q., Giangrande, S. E., Khain, A., Lin, Y., Mansell, E., Milbrandt, J. A., Stenz, R., Thompson, G., and Wang, Y.: Cloud-resolving model intercomparison of an MC3E squall line case:

Part I-Convective updrafts, J Geophys Res-Atmos, 122, 9351-9378, doi: 10.1002/2017jd026622, 2017.

Fan, J. W., Rosenfeld, D., Zhang, Y. W., Giangrande, S. E., Li, Z. Q., Machado, L. A. T., Martin, S. T., Yang, Y., Wang, J., Artaxo, P., Barbosa, H. M. J., Braga, R. C., Comstock, J. M., Feng, Z., Gao, W. H., Gomes, H. B., Mei, F., Pohlker, C., Pohlker, M. L., Poschl, U., and de Souza, R. A. F.: Substantial convection and precipitation enhancements by ultrafine aerosol particles, Science, 359, 411-418, doi: 10.1126/science.aan8461, 2018.

Fast, J. D., Gustafson, W. I., Easter, R. C., Zaveri, R. A., Barnard, J. C., Chapman, E. G., Grell, G. A., and Peckham, S. E.: Evolution of ozone, particulates, and aerosol direct radiative forcing in the vicinity of Houston using a fully coupled meteorology-chemistry-aerosol model, J Geophys Res-Atmos, 111, D21305, doi: 10.1029/2005jd006721, 2006.

Gao, W. H., Fan, J. W., Easter, R. C., Yang, Q., Zhao, C., and Ghan, S. J.: Coupling spectral-bin cloud microphysics with the MOSAIC aerosol model in WRF-Chem: Methodology and results for marine stratocumulus clouds, J Adv Model Earth Sy, 8, 1289-1309, doi: 10.1002/2016ms000676, 2016.

Gelaro, R., McCarty, W., Suarez, M. J., Todling, R., Molod, A., Takacs, L., Randles, C. A., Darmenov, A., Bosilovich, M. G., Reichle, R., Wargan, K., Coy, L., Cullather, R., Draper, C., Akella, S., Buchard, V., Conaty, A., da Silva, A. M., Gu, W., Kim, G. K., Koster, R., Lucchesi, R., Merkova, D., Nielsen, J. E., Partyka, G., Pawson, S., Putman, W., Rienecker, M., Schubert, S. D., Sienkiewicz, M., and Zhao, B.: The Modern-Era Retrospective Analysis for Research and Applications, Version 2 (MERRA-2), J Climate, 30, 5419-5454, doi: 10.1175/Jcli-D-16-0758.1, 2017.

589   Grabowski, W. W., and D.Jarecka: Modeling condensation in shallow nonprecipitating
590   convection. J. Atmos. Sci., 72, 4661–4679, 2015.

591   Grabowski, W. W., and H.Morrison: Untangling microphysical impacts on deep convection
592   applying a novel modeling methodology. Part II: Double-moment microphysics. J. Atmos.
593   Sci., 73, 3749–3770, 2016.

594   Grabowski, W. W., and H. Morrison: Modeling condensation in deep convection, J. Atmos.
595   Sci., 74, 2247– 2267, doi:10.1175/JAS-D-16-0255.1, 2017.

596   Grabowski, W. W., and H. Morrison: Do ultrafine cloud condensation nuclei invigorate deep
597   convection? J. Atmos. Sci., 77(7), 2567-2583, doi: 10.1175/JAS-D-20-0012.1, 2020.

598   Grell, G. A., Peckham, S. E., Schmitz, R., McKeen, S. A., Frost, G., Skamarock, W. C., and Eder,
599   B.: Fully coupled "online" chemistry within the WRF model, Atmos Environ, 39, 6957-
600   6975, doi: 10.1016/j.atmosenv.2005.04.027, 2005.

601   Guenther, A., Karl, T., Harley, P., Wiedinmyer, C., Palmer, P. I., and Geron, C.: Estimates of
602   global terrestrial isoprene emissions using MEGAN (Model of Emissions of Gases and
603   Aerosols from Nature), Atmos Chem Phys, 6, 3181-3210, doi: 10.5194/acp-6-3181-2006,
604   2006.

605   Haywood, J., and Boucher, O.: Estimates of the direct and indirect radiative forcing due to
606   tropospheric aerosols: A review, Rev Geophys, 38, 513-543, doi: 10.1029/1999rg000078,
607   2000.

608   Houze, R. A.: Cloud dynamics, 2. edn., Elsevier/Acad. Press, Amsterdam, 2014.

609   Iacono, M. J., Delamere, J. S., Mlawer, E. J., Shephard, M. W., Clough, S. A., and Collins, W. D.:
610   Radiative forcing by long-lived greenhouse gases: Calculations with the AER radiative
611   transfer models, J Geophys Res-Atmos, 113, D13103, doi: 10.1029/2008jd009944, 2008.

612   Janjic, Z. I.: The Step-Mountain Eta Coordinate Model - Further Developments of the Convection,

613   Viscous Sublayer, and Turbulence Closure Schemes, Mon Weather Rev, 122, 927-945, doi:

614   10.1175/1520-0493(1994)122<0927:Tsmecm>2.0.Co;2, 1994.

615   Khain, A., Pokrovsky, A., Pinsky, M., Seifert, A., and Phillips, V.: Simulation of effects of

616   atmospheric aerosols on deep turbulent convective clouds using a spectral microphysics

617   mixed-phase cumulus cloud model. Part I: Model description and possible applications, J

618   Atmos Sci, 61, 2963-2982, doi: 10.1175/Jas-3350.1, 2004.

619   Khain, A., Rosenfeld, D., and Pokrovsky, A.: Aerosol impact on the dynamics and microphysics

620   of deep convective clouds, Q J Roy Meteor Soc, 131, 2639-2663, doi: 10.1256/qj.04.62,

621   2005.

622   Khain, A., and Lynn, B.: Simulation of a supercell storm in clean and dirty atmosphere using

623   weather research and forecast model with spectral bin microphysics, J Geophys Res-Atmos,

624   114, D19209, doi: 10.1029/2009jd011827, 2009.

625   Khain, A., Lynn, B., and Dudhia, J.: Aerosol Effects on Intensity of Landfalling Hurricanes as

626   Seen from Simulations with the WRF Model with Spectral Bin Microphysics, J Atmos Sci,

627   67, 365-384, doi: 10.1175/2009jas3210.1, 2010.

628   Khain, A. P., BenMoshe, N., and Pokrovsky, A.: Factors determining the impact of aerosols on

629   surface precipitation from clouds: An attempt at classification, J Atmos Sci, 65, 1721-1748,

630   doi: 10.1175/2007jas2515.1, 2008.

631   Khain, A. P., Leung, L. R., Lynn, B., and Ghan, S.: Effects of aerosols on the dynamics and

632   microphysics of squall lines simulated by spectral bin and bulk parameterization schemes,

633   J Geophys Res-Atmos, 114, D22203, doi: 10.1029/2009jd011902, 2009.

634   Khain, A. P., Beheng, K. D., Heymsfield, A., Korolev, A., Krichak, S. O., Levin, Z., Pinsky, M.,

635   Phillips, V., Prabhakaran, T., Teller, A., van den Heever, S. C., and Yano, J. I.:

636   Representation of microphysical processes in cloud-resolving models: Spectral (bin)

637   microphysics versus bulk parameterization, Rev Geophys, 53, 247-322, doi:

638   10.1002/2014rg000468, 2015.

639   Koren, I., Dagan, G., and Altaratz, O.: From aerosol-limited to invigoration of warm convective

640   clouds, Science, 344, 1143-1146, doi: 10.1126/science.1252595, 2014.

641   Korolev A., and I. Mazin: Supersaturation of water vapor in clouds. J. Atmos. Sci., 60, 2957-2974,

642   2003.

643   Lebo, Z.: A Numerical Investigation of the Potential Effects of Aerosol-Induced Warming and

644   Updraft Width and Slope on Updraft Intensity in Deep Convective Clouds, J Atmos Sci,

645   75, 535-554, doi: 10.1175/Jas-D-16-0368.1, 2018.

646   Lebo, Z. J., and Seinfeld, J. H.: Theoretical basis for convective invigoration due to increased

647   aerosol concentration, Atmos Chem Phys, 11, 5407-5429, doi: 10.5194/acp-11-5407-2011,

648   2011.

649   Lebo, Z. J., Morrison, H., and Seinfeld, J. H.: Are simulated aerosol-induced effects on deep

650   convective clouds strongly dependent on saturation adjustment? Atmos Chem Phys, 12,

651   9941-9964, doi: 10.5194/acp-12-9941-2012, 2012.

652   Lee, S. S., Li, Z. Q., Zhang, Y. W., Yoo, H., Kim, S., Kim, B. G., Choi, Y. S., Mok, J., Um, J.,

653   Choi, K. O., and Dong, D. H.: Effects of model resolution and parameterizations on the

654   simulations of clouds, precipitation, and their interactions with aerosols, Atmos Chem Phys,

655   18, 13-29, doi: 10.5194/acp-18-13-2018, 2018.

656 Li, G. H., Wang, Y., and Zhang, R. Y.: Implementation of a two-moment bulk microphysics

657   scheme to the WRF model to investigate aerosol-cloud interaction, J Geophys Res-Atmos,

658   113, D15211, doi: 10.1029/2007jd009361, 2008.

659 Li, X. W., Tao, W. K., Khain, A. P., Simpson, J., and Johnson, D. E.: Sensitivity of a Cloud-

660   Resolving Model to Bulk and Explicit Bin Microphysical Schemes. Part I: Comparisons, J

661   Atmos Sci, 66, 3-21, doi: 10.1175/2008jas2646.1, 2009.

662 Li, Z. Q., Niu, F., Fan, J. W., Liu, Y. G., Rosenfeld, D., and Ding, Y. N.: Long-term impacts of

663   aerosols on the vertical development of clouds and precipitation, Nat Geosci, 4, 888-894,

664   doi: 10.1038/Ngeo1313, 2011.

665 Loftus, A. M., and Cotton, W. R.: Examination of CCN impacts on hail in a simulated supercell

666   storm with triple-moment hail bulk microphysics, Atmos Res, 147, 183-204, doi:

667   10.1016/j.atmosres.2014.04.017, 2014.

668 Lohmann, U., and Feichter, J.: Global indirect aerosol effects: a review, Atmos Chem Phys, 5,

669   715-737, doi: 10.5194/acp-5-715-2005, 2005.

670 Milbrandt, J. A., and Yau, M. K.: A multimoment bulk microphysics parameterization. Part II: A

671   proposed three-moment closure and scheme description, J Atmos Sci, 62, 3065-3081, doi:

672   10.1175/Jas3535.1, 2005.

673 Morrison, H., Curry, J. A., and Khvorostyanov, V. I.: A new double-moment microphysics

674   parameterization for application in cloud and climate models. Part I: Description, J Atmos

675   Sci, 62, 1665-1677, doi: 10.1175/Jas3446.1, 2005.

676 Morrison, H., and W. W.Grabowski: Comparison of bulk and bin warm-rain microphysics models

677   using a kinematic framework.J. Atmos. Sci., 64, 2839–2861, 2007.

678   Morrison, H., and W. W. Grabowski: Modeling supersaturation and subgrid-scale mixing with

679   two-moment bulk warm microphysics, J. Atmos. Sci., 65, 792–812,

680   doi:10.1175/2007JAS2374.1, 2008.

681   Morrison, H., Thompson, G., and Tatarskii, V.: Impact of Cloud Microphysics on the Development

682   of Trailing Stratiform Precipitation in a Simulated Squall Line: Comparison of One- and

683   Two-Moment Schemes, Mon Weather Rev, 137, 991-1007, doi: 10.1175/2008mwr2556.1,

684   2009.

685   Morrison, H., and Milbrandt, J.: Comparison of Two-Moment Bulk Microphysics Schemes in

686   Idealized Supercell Thunderstorm Simulations, Mon Weather Rev, 139, 1103-1130, doi:

687   10.1175/2010mwr3433.1, 2011.

688   Morrison, H.: On the robustness of aerosol effects on an idealized supercell storm simulated with

689   a cloud system-resolving model, Atmos Chem Phys, 12, 7689-7705, doi: 10.5194/acp-12-

690   7689-2012, 2012.

691   Pinsky M., I.P. Mazin, A. Korolev, and A.P. Khain: Supersaturation and diffusional droplet growth

692   in liquid clouds. J. Atmos. Sci. 70, 2778-2793, 2013.

693   Politovich, M. K., and W. A. Cooper: Variability of the supersaturation in cumulus clouds. J.

694   Atmos. Sci., 45, 1651–1664, doi:10.1175/1520-0469(1988)045,1651:VOTSIC.2.0.CO;2,

695   1988.

696   Rosenfeld, D., Lohmann, U., Raga, G. B., O'Dowd, C. D., Kulmala, M., Fuzzi, S., Reissell, A.,

697   and Andreae, M. O.: Flood or drought: How do aerosols affect precipitation?, Science, 321,

698   1309-1313, doi: 10.1126/science.1160606, 2008.

699   Rosenfeld, D., Andreae, M. O., Asmi, A., Chin, M., de Leeuw, G., Donovan, D. P., Kahn, R.,

700   Kinne, S., Kivekas, N., Kulmala, M., Lau, W., Schmidt, K. S., Suni, T., Wagner, T., Wild,

701   M., and Quaas, J.: Global observations of aerosol-cloud-precipitation-climate interactions,

702   Rev Geophys, 52, 750-808, doi: 10.1002/2013rg000441, 2014.

703 Rosenfeld, D., Zheng, Y. T., Hashimshoni, E., Pohlker, M. L., Jefferson, A., Pohlker, C., Yu, X.,

704   Zhu, Y. N., Liu, G. H., Yue, Z. G., Fischman, B., Li, Z. Q., Giguzin, D., Goren, T., Artaxo,

705   P., Barbosa, H. M. J., Poschl, U., and Andreae, M. O.: Satellite retrieval of cloud

706   condensation nuclei concentrations by using clouds as CCN chambers, P Natl Acad Sci

707   USA, 113, 5828-5834, doi: 10.1073/pnas.1514044113, 2016.

708 Salamanca, F., and Martilli, A.: A new Building Energy Model coupled with an Urban Canopy

709   Parameterization for urban climate simulations-part II. Validation with one dimension off-

710   line simulations, Theor Appl Climatol, 99, 345-356, doi: 10.1007/s00704-009-0143-8,

711   2010.

712 Sheffield, A. M., Saleeby, S. M., and van den Heever, S. C.: Aerosol-induced mechanisms for

713   cumulus congestus growth, J Geophys Res-Atmos, 120, 8941-8952, doi:

714   10.1002/2015jd023743, 2015.

715 Skamarock, W. C., Klemp, J. B., Dudhia, J., Gill, D. O., Barker, D. M., Duda, M., Huang, X. Y.,

716   Wang, W., and Powers, J. G.: A description of the advanced research WRF version 3,

717   NCAR, Tech. Note, Mesoscale and Microscale Meteorology Division, National Center for

718   Atmospheric Research, Boulder, Colorado, USA, 2008.

719 Stevens, B., and G.Feingold: Untangling aerosol effects on clouds and precipitation in a buffered

720   system. Nature, 461, 607–613, 2009.

721 Storer, R. L., van den Heever, S. C., and Stephens, G. L.: Modeling Aerosol Impacts on Convective

722   Storms in Different Environments, J Atmos Sci, 67, 3904-3915, doi:

723   10.1175/2010jas3363.1, 2010.

724 Tao, W., and X. Li: The relationship between latent heating, vertical velocity, and precipitation

725   processes: The impact of aerosols on precipitation in organized deep convective systems,

726   J. Geophys. Res. Atmos., 121(11), 6299-6320, 2016.

727 Varble A.: Erroneous attribution of deep convective invigoration to aerosol concentration. J Atmos

728   Sci, 75(4):1351–68, 2018.

729 van den Heever, S. C., G. L.Stephens, and N. B.Wood: Aerosol indirect effects on tropical

730   convection characteristics under conditions of radiative-convective equilibrium. J. Atmos.

731   Sci., 68, 699–718, 2011.

732 Wang, Y., Fan, J. W., Zhang, R. Y., Leung, L. R., and Franklin, C.: Improving bulk microphysics

733   parameterizations in simulations of aerosol effects, J Geophys Res-Atmos, 118, 5361-5379,

734   doi: 10.1002/jgrd.50432, 2013.

735 Wiedinmyer, C., Akagi, S. K., Yokelson, R. J., Emmons, L. K., Al-Saadi, J. A., Orlando, J. J., and

736   Soja, A. J.: The Fire INventory from NCAR (FINN): a high resolution global model to

737   estimate the emissions from open burning, Geosci Model Dev, 4, 625-641, doi:

738   10.5194/gmd-4-625-2011, 2011.

739 Yuan, T. L., Li, Z. Q., Zhang, R. Y., and Fan, J. W.: Increase of cloud droplet size with aerosol

740   optical depth: An observation and modeling study, J Geophys Res-Atmos, 113, D04201,

741   doi: 10.1029/2007jd008632, 2008.

742 Zaveri, R. A., Easter, R. C., Fast, J. D., and Peters, L. K.: Model for Simulating Aerosol

743   Interactions and Chemistry (MOSAIC), J Geophys Res-Atmos, 113, D13204, doi:

744   10.1029/2007jd008782, 2008.

745

746   **Table 1** Descriptions of the PM2.5 Monitoring Sites over the Houston area from TCEQ

Abbreviation	Site Descriptions	Latitude	Longitude
HA	Houston Aldine	29.901	-95.326
HDP	Houston Deer Park 2	29.670	-95.129
SFP	Seabrook Friendship Park	29.583	-95.016
CR	Conroe Relocated	30.350	-95.425
KW	Kingwood	30.058	-95.190
CT	Clinton	29.734	-95.258
PP	Park Place	29.686	-95.294
GS	Galveston 99th Street	29.254	-94.861

747

748

749
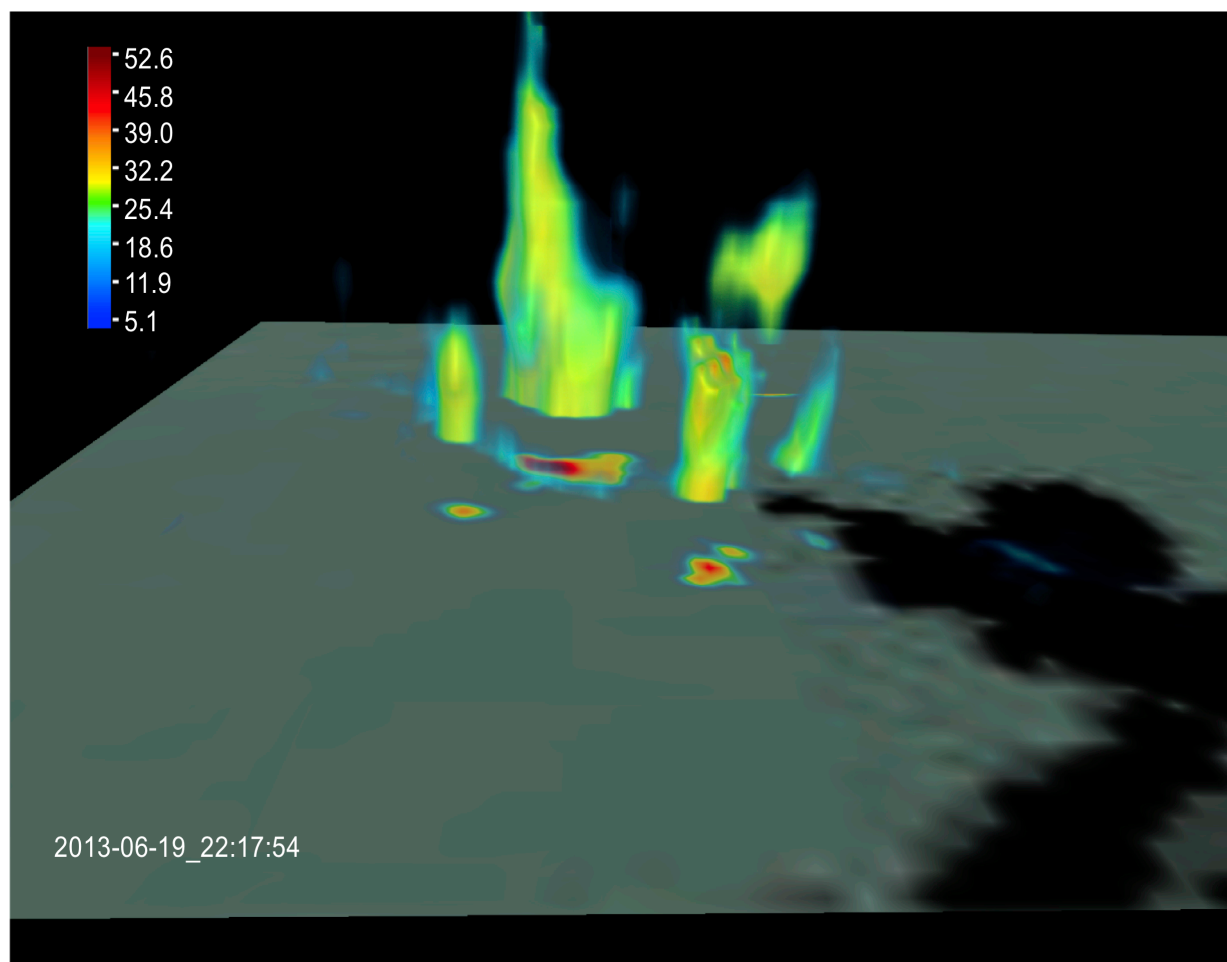
Figure 1 3D structure snapshot of radar reflectivity (unit: dBZ) from NEXRAD, overlaid with the composite reflectivity shown on the surface at the time when the maximum reflectivity is observed (2217 UTC). The dark shade shows the water body and the largest cell is in the Houston.
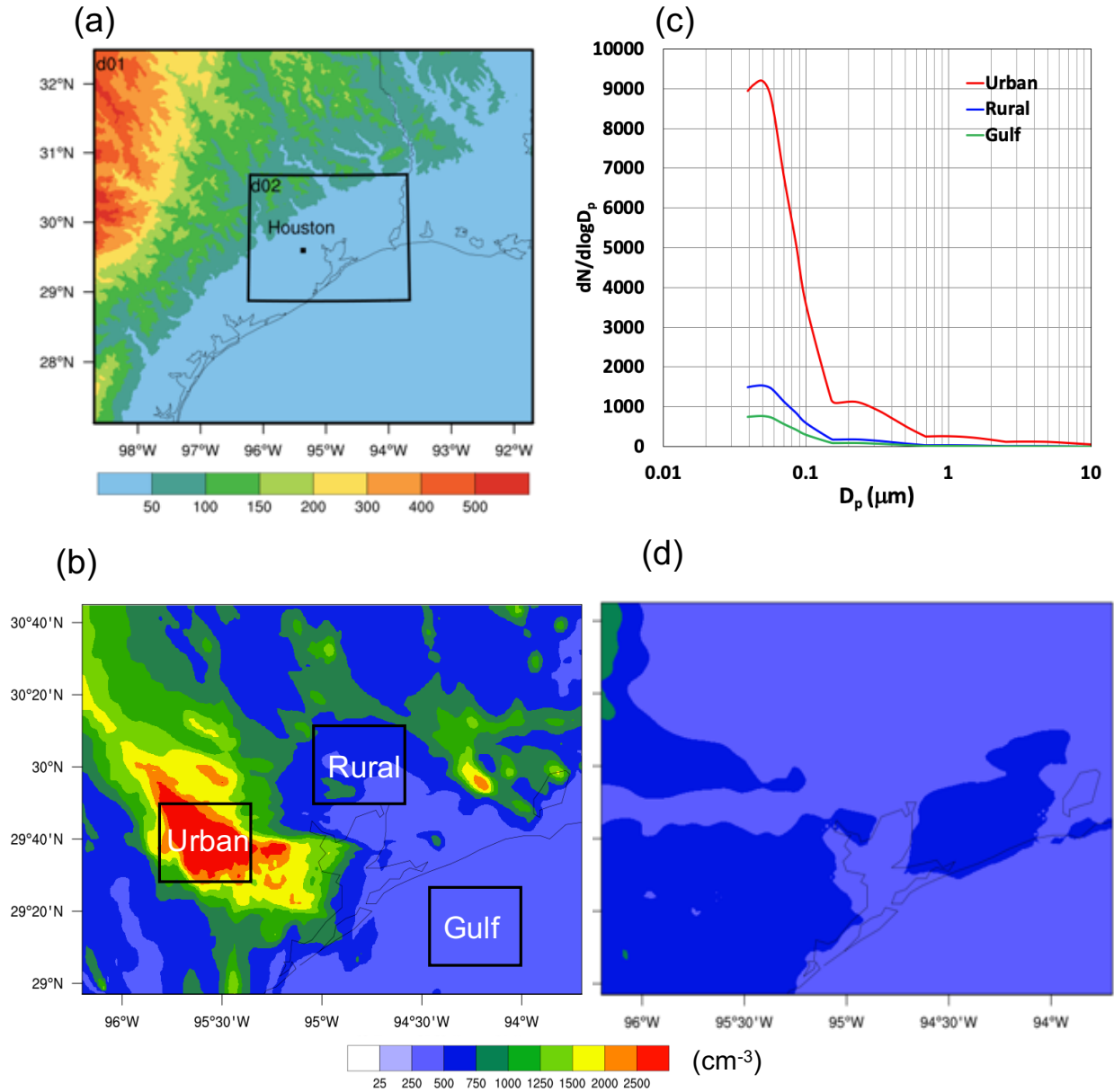
Figure 2 (a) Simulation domains with the terrain heights (unit: m), (b) aerosol number concentration (unit: cm^{-3}) from D1_MOR_anth, (c) aerosol size distributions over the urban, rural, and Gulf of Mexico as marked by three black boxes in Fig. 2b at 1200 UTC, 19 Jun 2013 (6-hr before the convection initiation), and (d) the same as Fig. 2b, but for D1_MOR_noanth in which the anthropogenic aerosols are excluded.

762
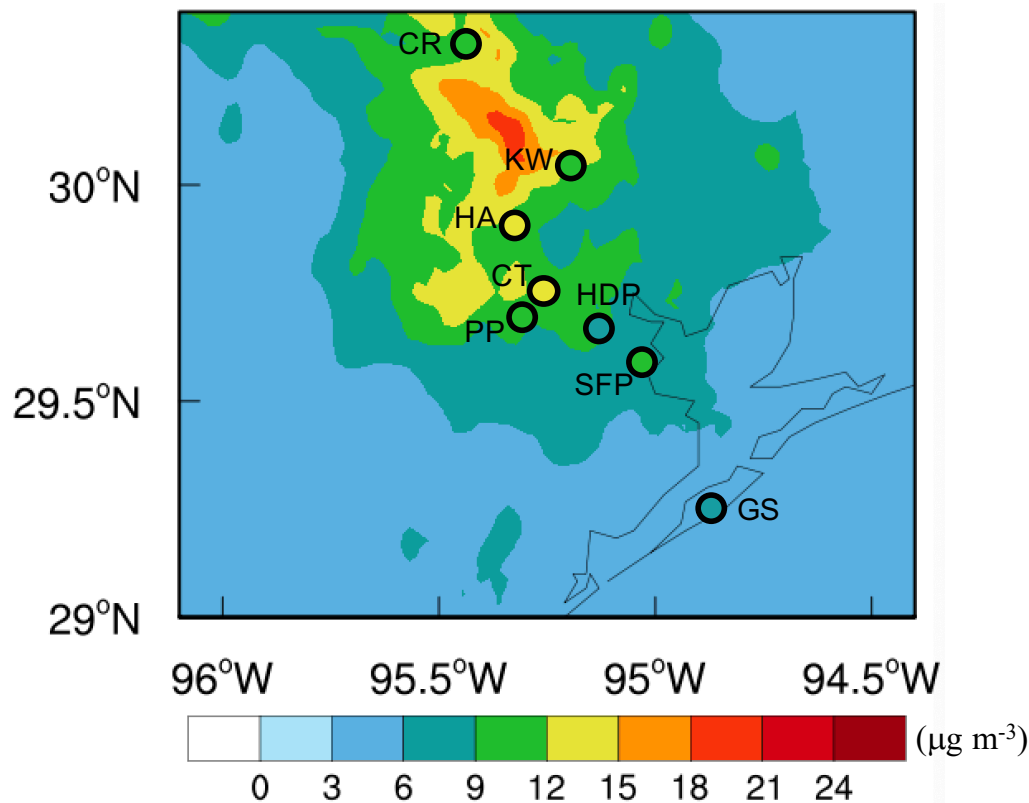
Figure 3 Comparisons of 24-hr averaged PM2.5 mass concentrations (unit: μg m^{-3}) between model
simulation D1_MOR_anth (contoured) and site observation from TCEQ (colored circles) from
1800 UTC, 18 June 2013 to 1800 UTC, 19 June 2013 (1 day before the convection initiation). The
site names and other information are shown in Table 1.
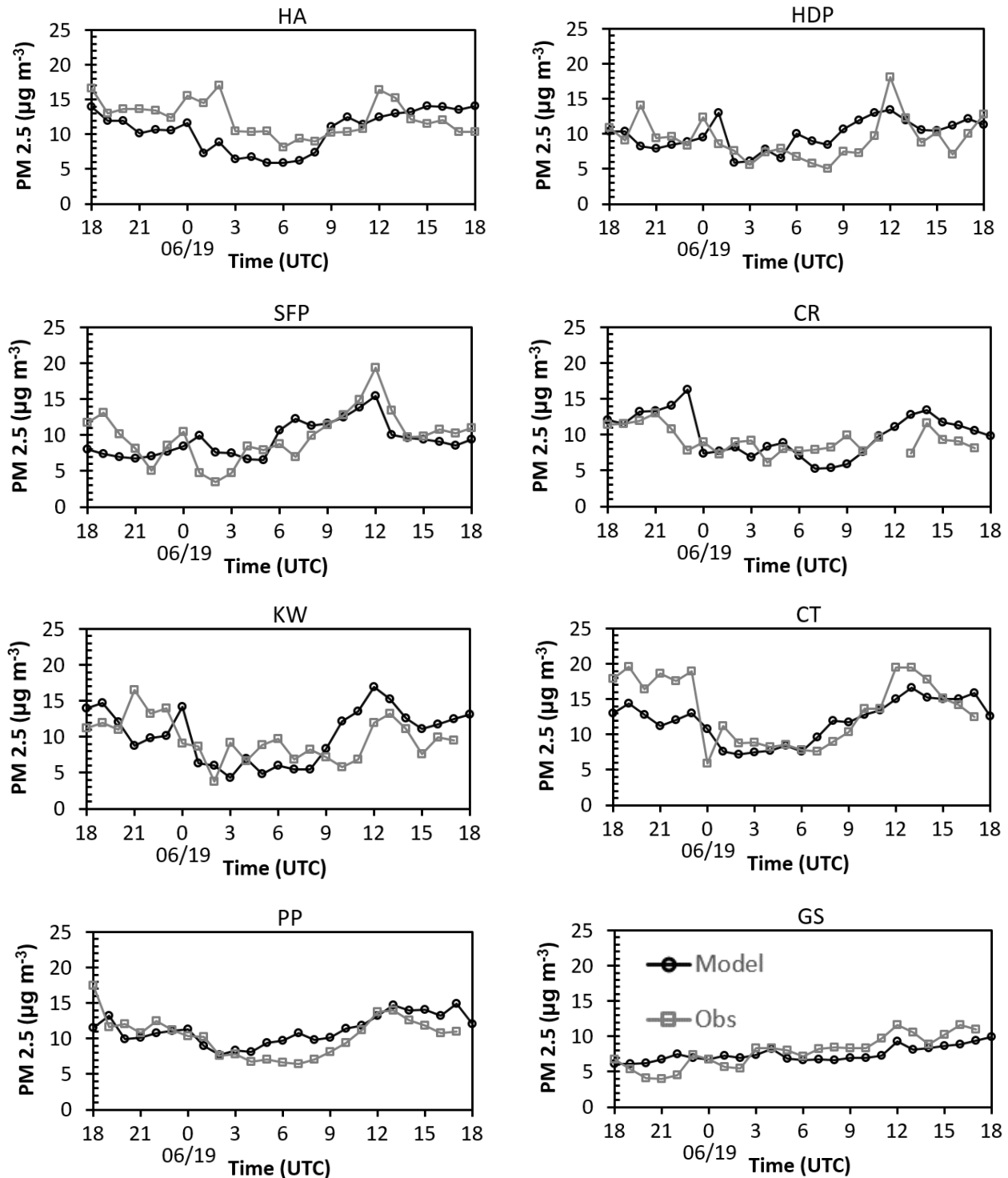
Figure 4 Site-by-site comparisons of hourly PM2.5 mass concentrations (unit: μg m⁻³) from D1_MOR_anth and TCEQ site observation over 24 hours from 1800 UTC, 18 June 2013 to 1800 UTC, 19 June 2013 (1 day before the convection initiation).
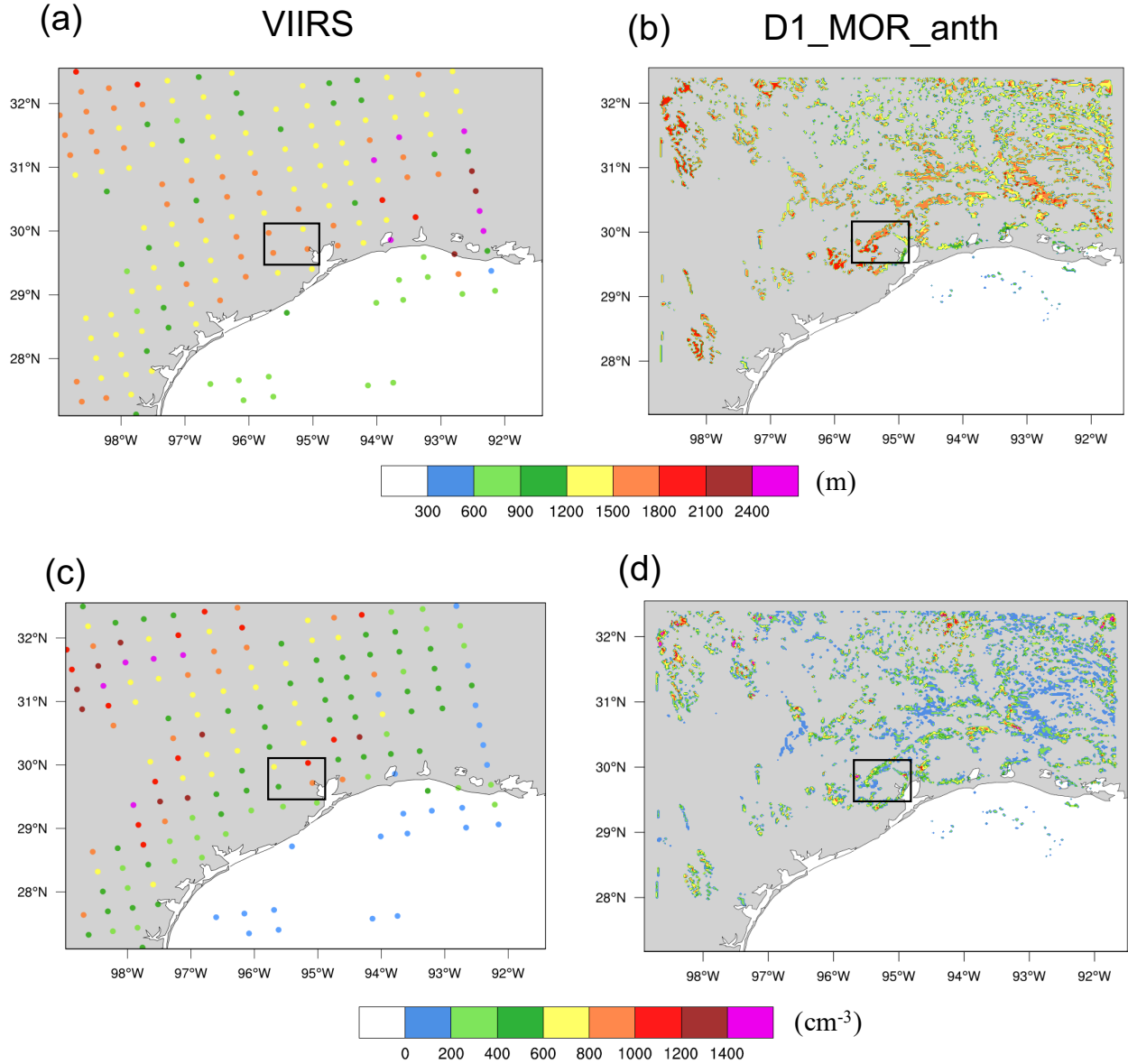
Figure 5 Evaluation of (a,b) cloud base heights (unit: m) and (c,d) CCN number concentration at cloud base (unit: cm^{-3}) from VIIRS satellite (left) retrieved at 1943 UTC (Rosenfeld et al. 2016) and model simulation D1_MOR_anth (right) at 2000 UTC, 19 June 2013. The Houston area is marked as the black box. Satellite-retrieved cloud base height was calculated from the difference between reanalysis surface air temperature (from reanalysis data) and VIIRS-measured cloud base temperature (warmest cloudy pixel) divided by the dry adiabatic lapse rate, while modeled cloud base height was determined by the lowest cloud layer with cloud mass mixing ratio greater than 10^{-5} kg kg^{-1}.
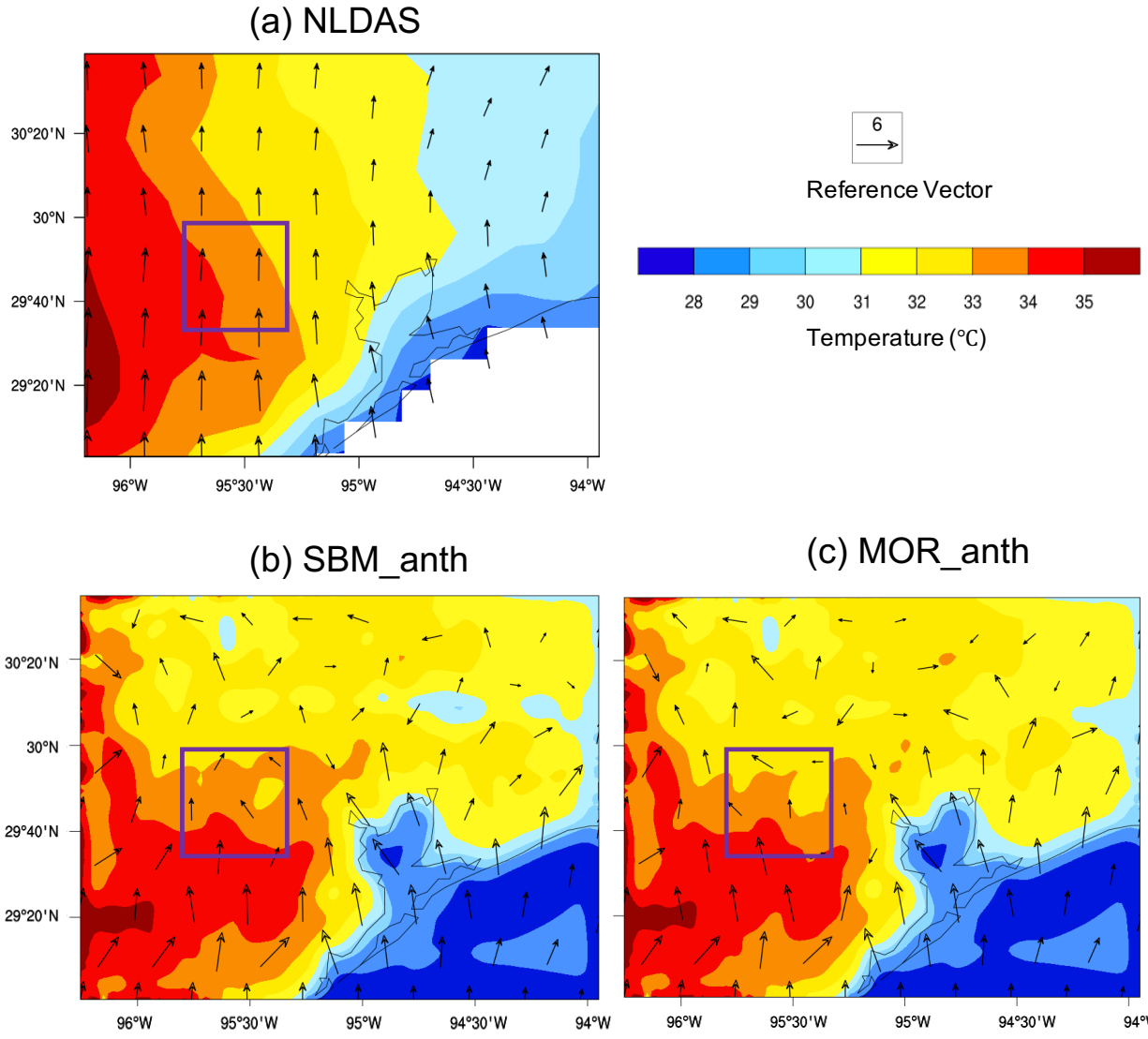
Figure 6 2-m Temperature (shaded; unit: °C) and 10-m winds (vectors; unit: m s^{-1}) from (a) NLDAS, (b) SBM_anth and (c) MOR_anth at 1800 UTC, 19 Jun 2013. The purple box denotes the Houston area.

787
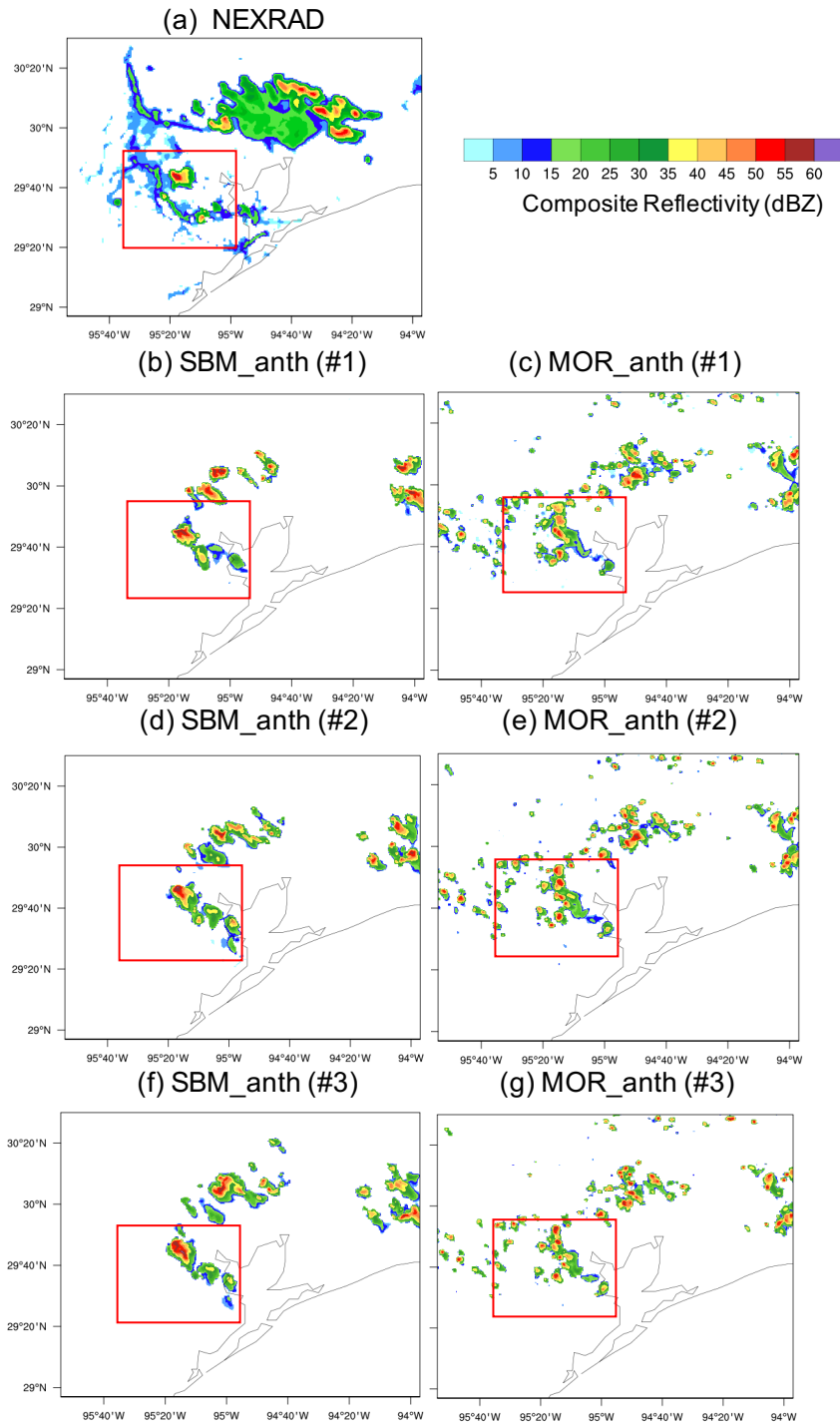
Figure 7 Composite reflectivity (unit: dBZ) from (a) NEXRAD (2217 UTC), (b, d, f) three
ensemble runs for SBM_anth (2140 UTC) and (c, e, g) three ensemble runs for MOR_anth (2125
UTC) when maximum reflectivity in Houston is observed on 19 June 2013. The red box is the
study area for convection cells near Houston.

792
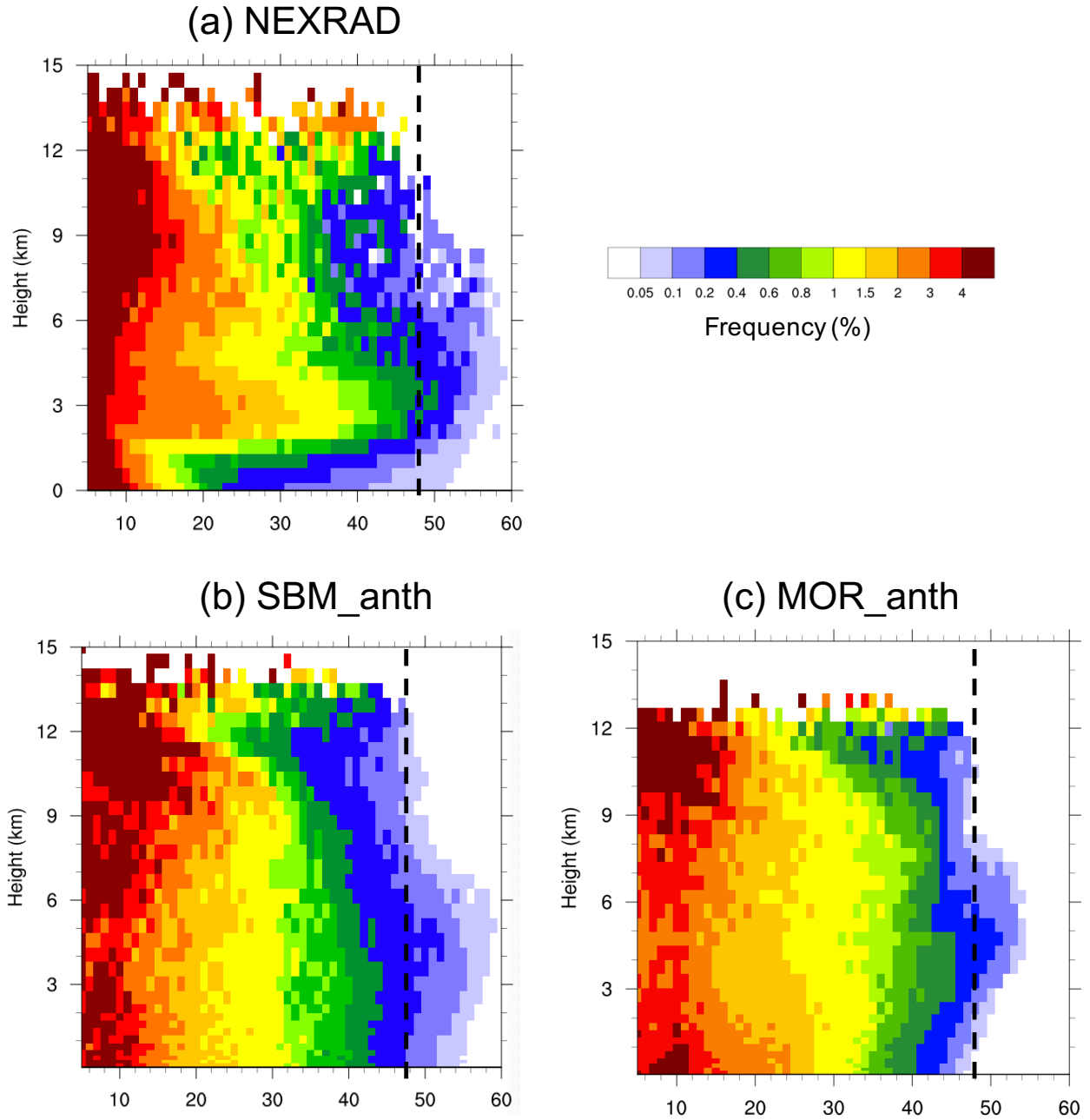
Figure 8 The CFAD of reflectivity (unit: dBZ) for the values larger than 0 dBZ from (a) NEXRAD, (b) SBM_anth and (c) MOR_anth over the study area (red box in Fig. 7) from 1800 UTC, 19 Jun to 0000 UTC, 20 Jun 2013. The black solid lines denote the reflectivity with the value of 48 dBZ. The results are the three ensemble means.

(a)

(b)

799
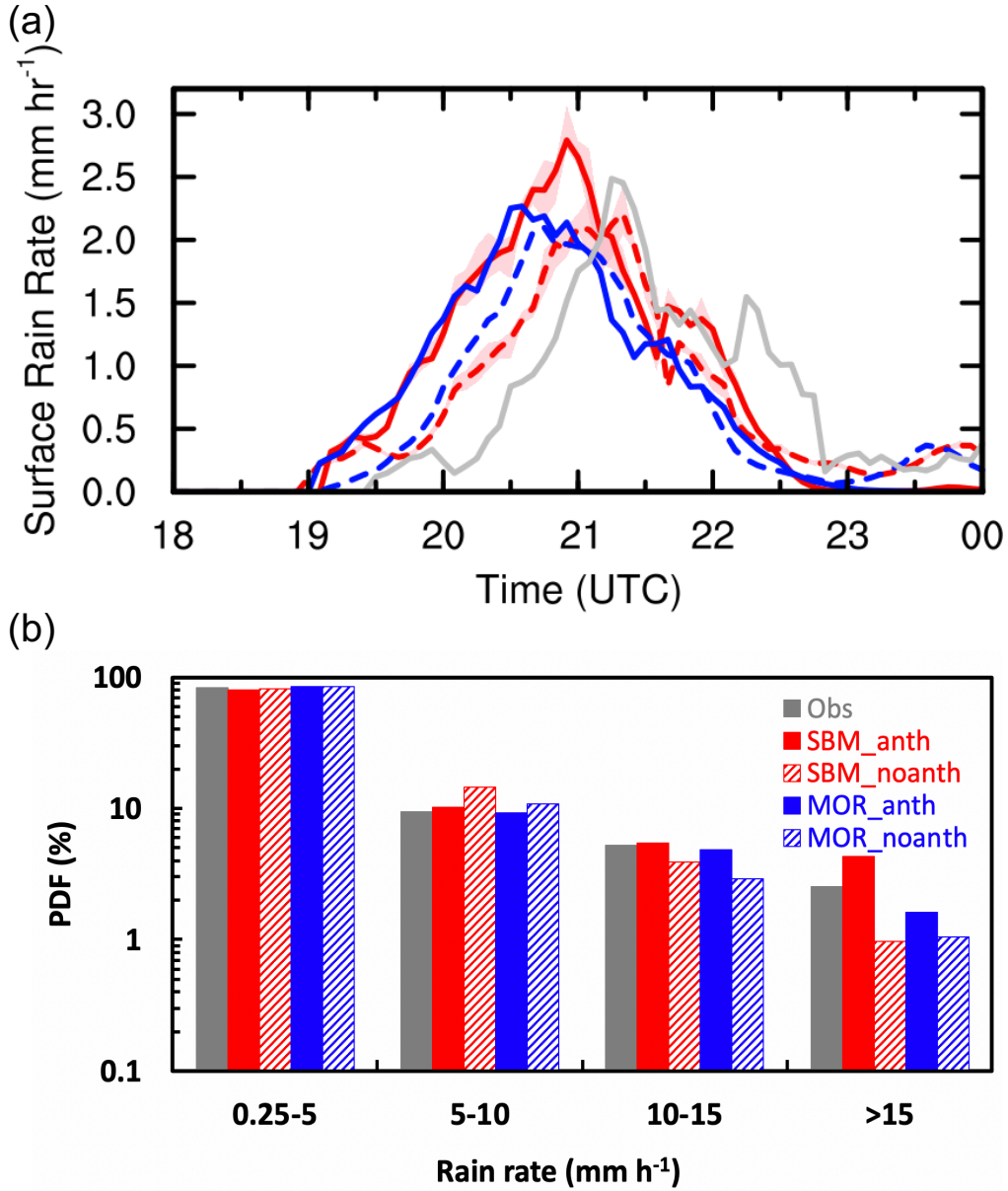
Figure 9 (a) Time series of averaged surface rain rate (unit: mm h^{-1}) and (b) PDFs of rain rate for
the values larger than 0.25 mm h^{-1} over the study area (red box in Fig. 7) from observation (grey),
SBM_anth and SBM_noanth (red), MOR_anth and MOR_noanth (blue) from 1800UTC, 19 Jun
2013 to 0000 UTC, 20 Jun 2013. The observed precipitation rate is obtained by NEXRAD
retrieved rain rate. Both observation and model data are in every 5-min frequency. The results are
the three ensemble means. The shaded areas mark the spread of the ensemble members.

806

807

808
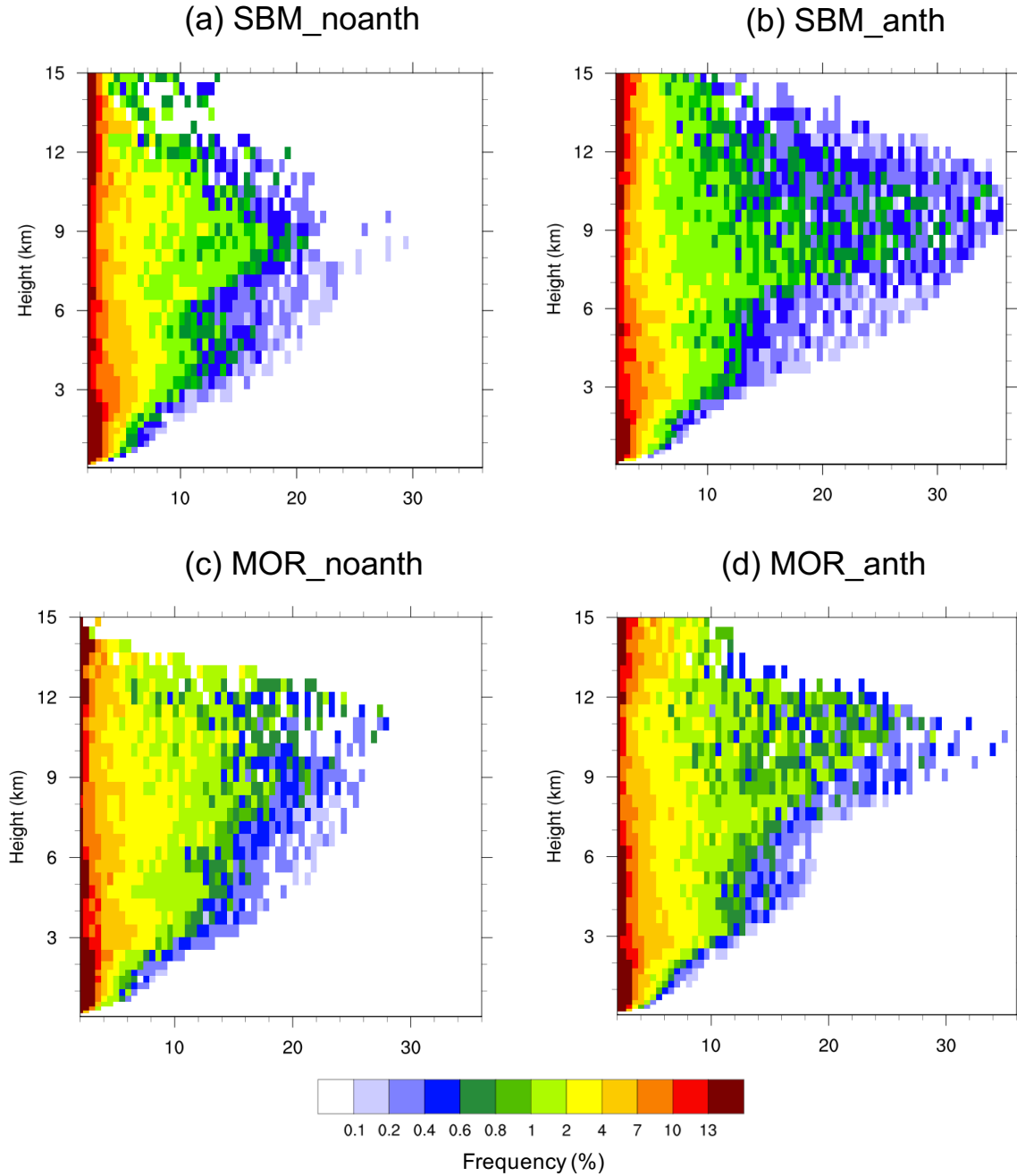
Figure 10 CFADs of updraft velocity (unit: m s^{-1}) for values larger than 2 m s^{-1} from (a) SBM_noanth, (b) SBM_anth, (c) MOR_noanth, and (d) MOR_anth over the study area (red box in Fig. 7) during the strong convection period (2000 – 2300 UTC, 19 Jun 2013). The results are the three ensemble means.

814
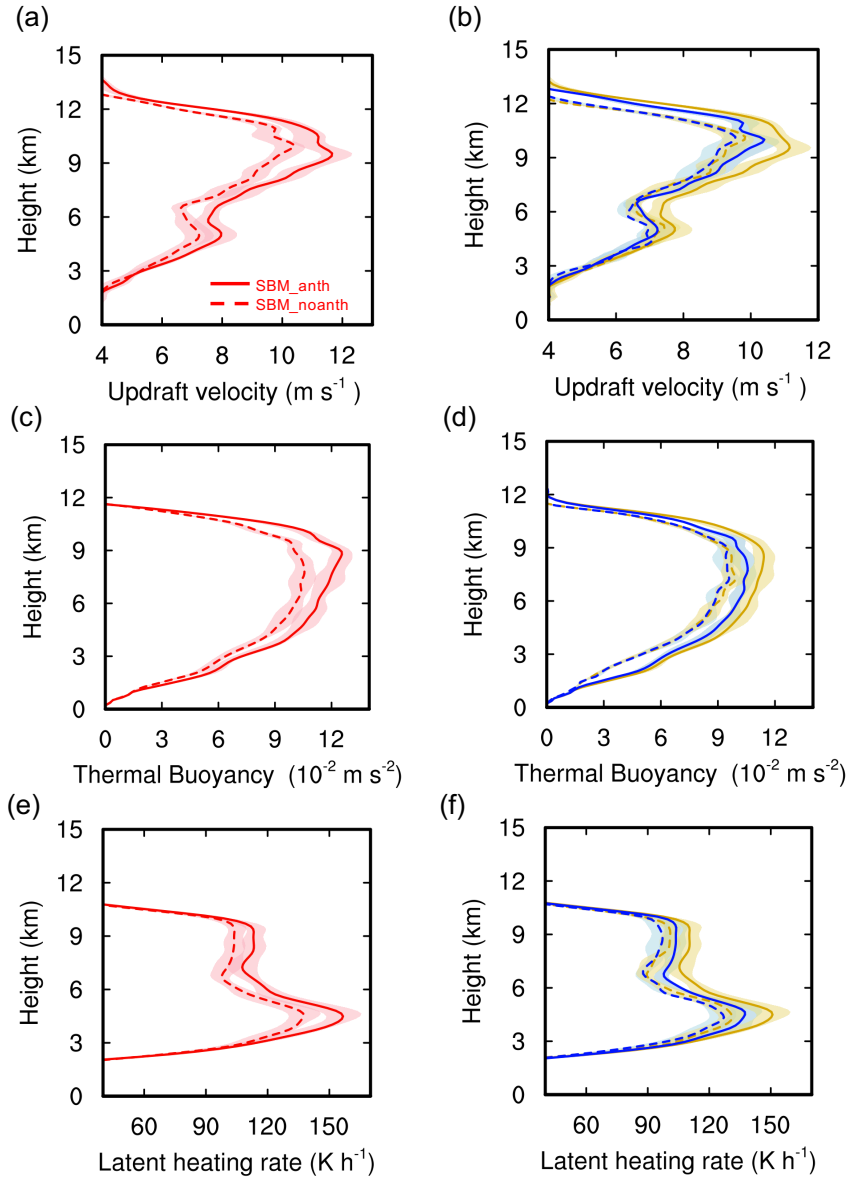
Figure 11 Vertical profiles of (a,b) updraft velocity (unit: m s^{-1}) , (c,d) thermal buoyancy (unit: m s^{-2}) and (e,f) total latent heating rate (unit: K h^{-1}) averaged over the top 25 percentiles (i.e., from 75th to 100th) of the updrafts with velocity greater than 2 m s^{-1} from the simulations SBM_anth and SBM_noanth (red), MOR_anth and MOR_noanth (blue), and MOR_SS_anth and MOR_SS_noanth (orange) over the study area (red box in Fig. 7) during the strong convection period (2000 – 2300 UTC, 19 Jun 2013). The results are the three ensemble means. The shaded areas mark the spread of the ensemble members.

822
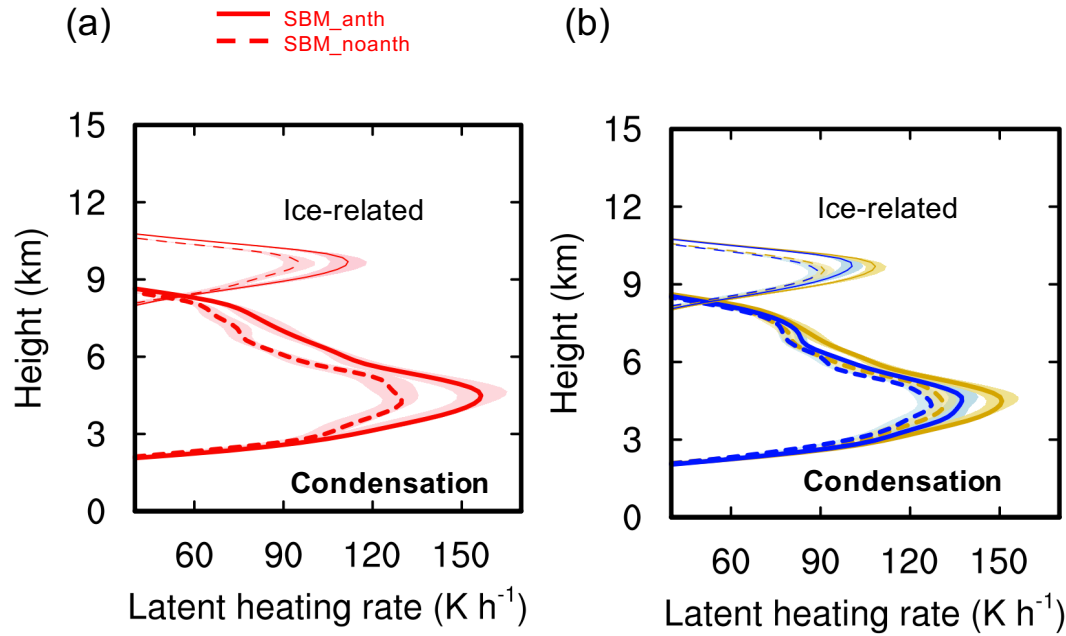
Figure 12 Vertical profiles of condensation heating rate (thick lines below 9 km; unit: K h^{-1}) and ice-related latent heating rate (thin lines above 9 km; unit: K h^{-1}) averaged over the top 25 percentiles (i.e., 75th to 100th) of the updrafts with velocity greater than 2 m s^{-1} from the simulations (a) SBM_anth and SBM_noanth (red), and (b) MOR_anth and MOR_noanth (blue), and MOR_SS_anth and MOR_SS_noanth (orange) over the study area (red box in Fig. 7) during the strong convection period (2000 – 2300 UTC, 19 Jun 2013). Data are processed in the same way as Figure 11.
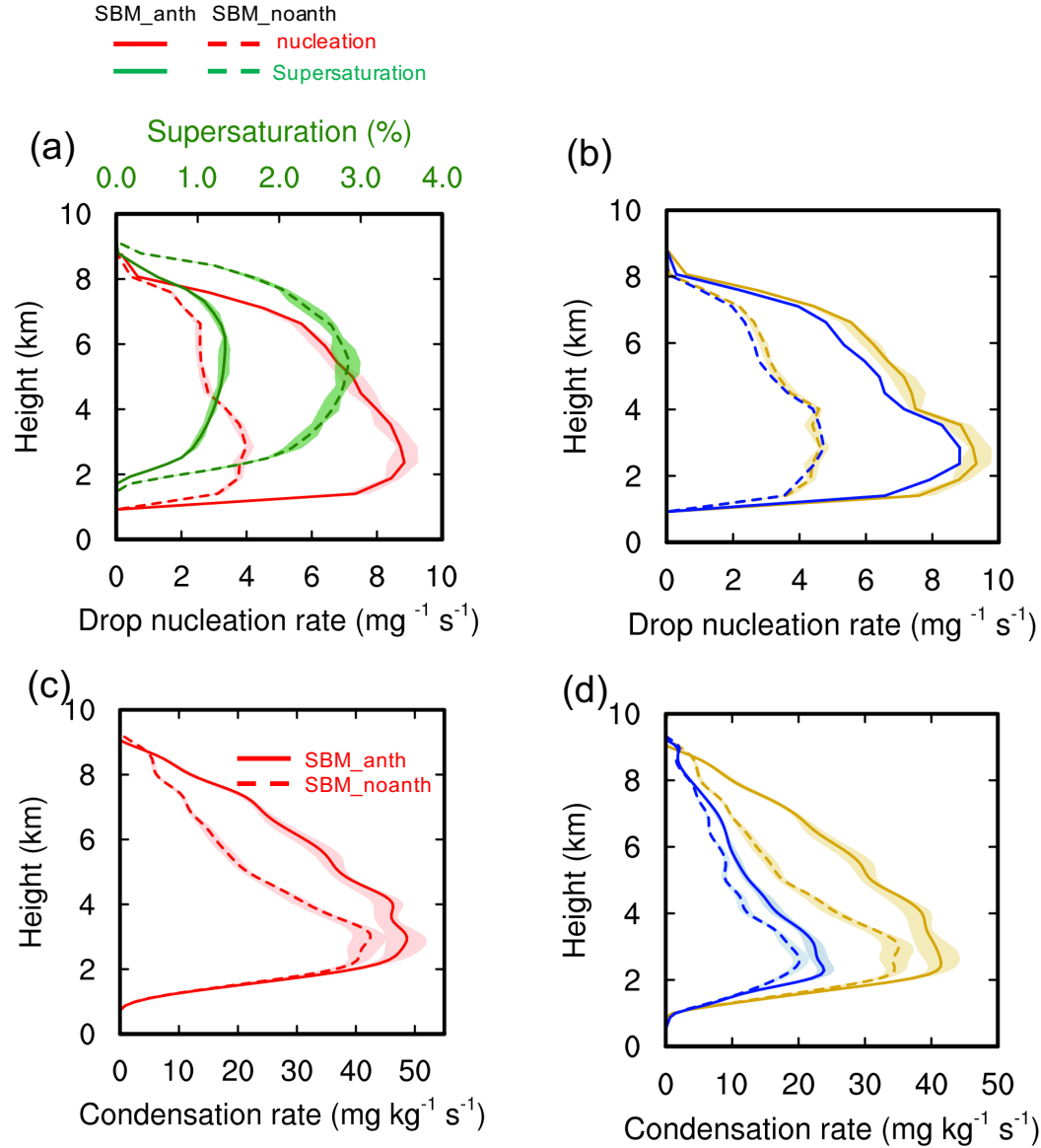
Figure 13 Vertical profiles of (a) drop nucleation rate (red; unit: $mg^{-1}\,s^{-1}$) and supersaturation with respect to water (green; unit: %) from SBM_anth and SBM_noanth, (b) drop nucleation rate (unit: $mg^{-1}\,s^{-1}$) from MOR_anth and MOR_noanth (blue), and MOR_SS_anth and MOR_SS_noanth (orange), (c) condensation rate (unit: $mg\,kg^{-1}\,s^{-1}$) from SBM_anth and SBM_noanth (red), and (d) the same as (c) but from MOR_anth and MOR_noanth (blue), and MOR_SS_anth and MOR_SS_noanth (orange), averaged over the top 25 percentiles (i.e., from 75th to 100th) of the updrafts with velocity greater than 2 m s^{-1} over the study area (red box in Fig. 7) during the strong convection period (2000 – 2300 UTC, 19 Jun 2013). Data are processed in the same way as Figure 11.
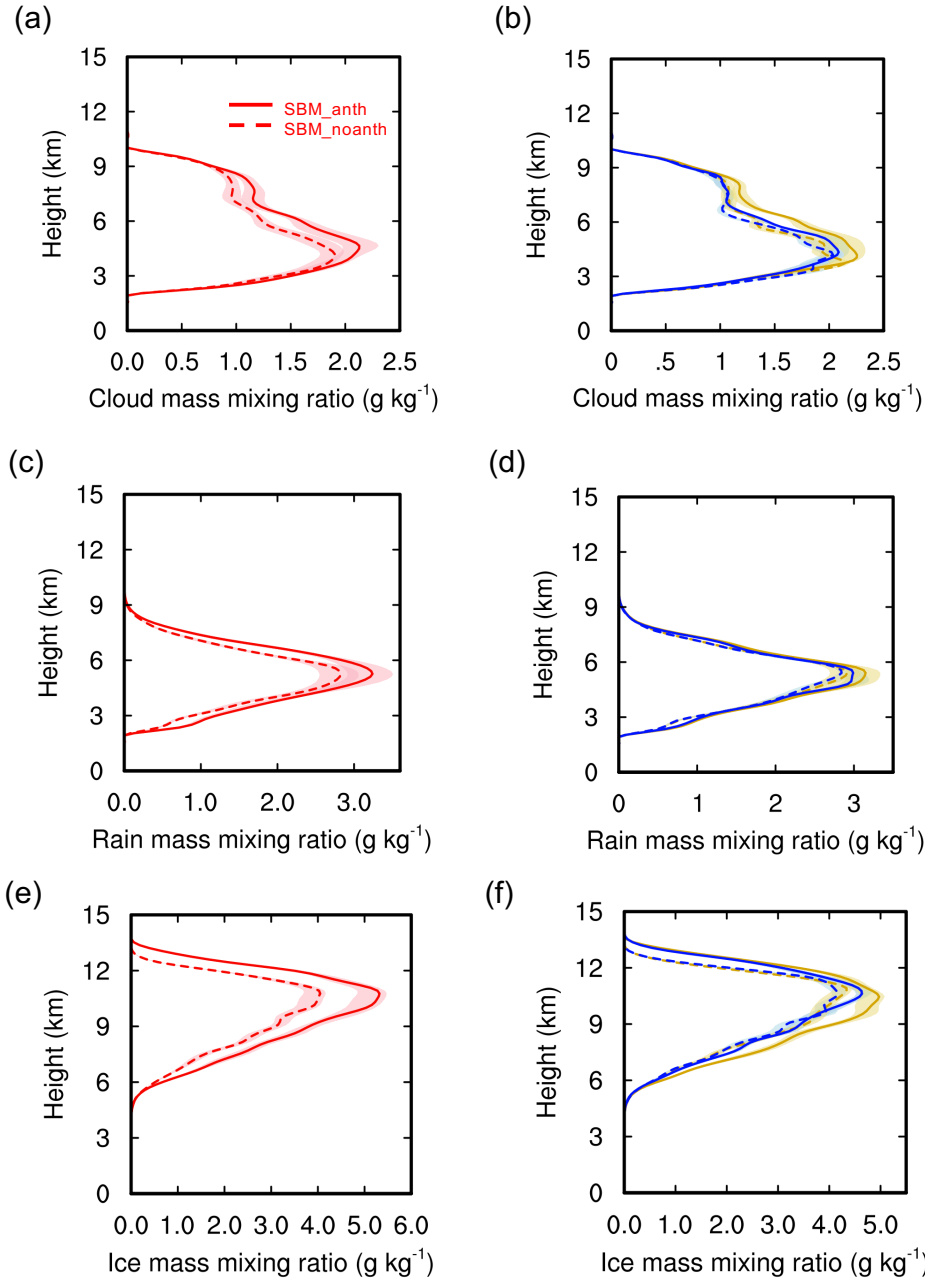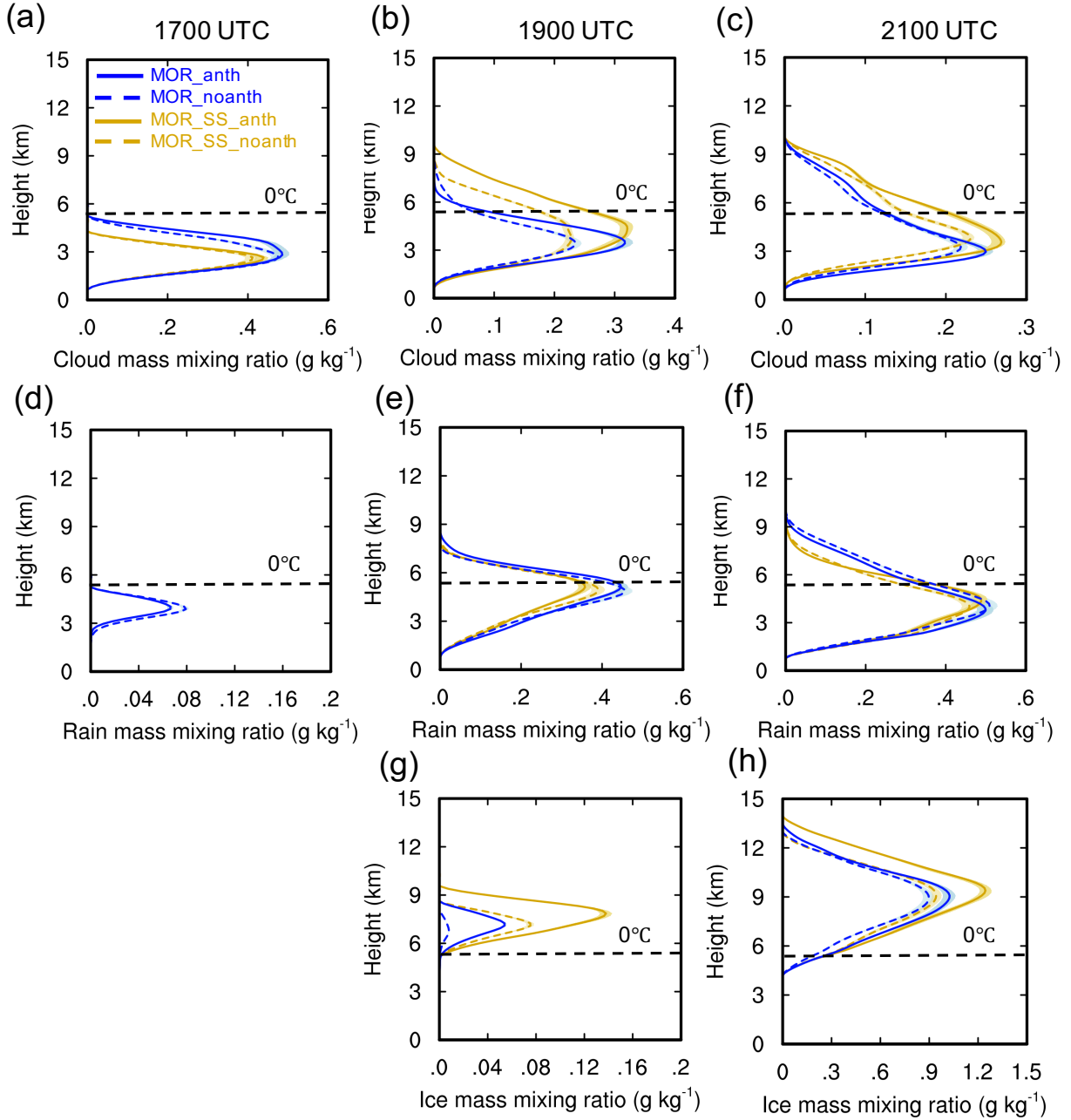
Figure 14 Vertical profiles of (a, b) cloud droplet, (c, d) rain drop and (e, f) ice particle (including ice, snow, and graupel) mass mixing ratios (unit: g kg^{-1}) averaged over the top 25 percentiles (i.e., 75th to 100th) of the updrafts with value greater than 2 m s^{-1} from the simulations SBM_anth and SBM_noanth (red), MOR_anth and MOR_noanth (blue), and MOR_SS_anth and MOR_SS_noanth (orange) over the study area (red box in Fig. 7) during the strong convection period (2000 – 2300 UTC, 19 Jun 2013). Data are processed in the same way as Figure 11.

(a)

(b)

(c)

(d)

(e)

(f)

850
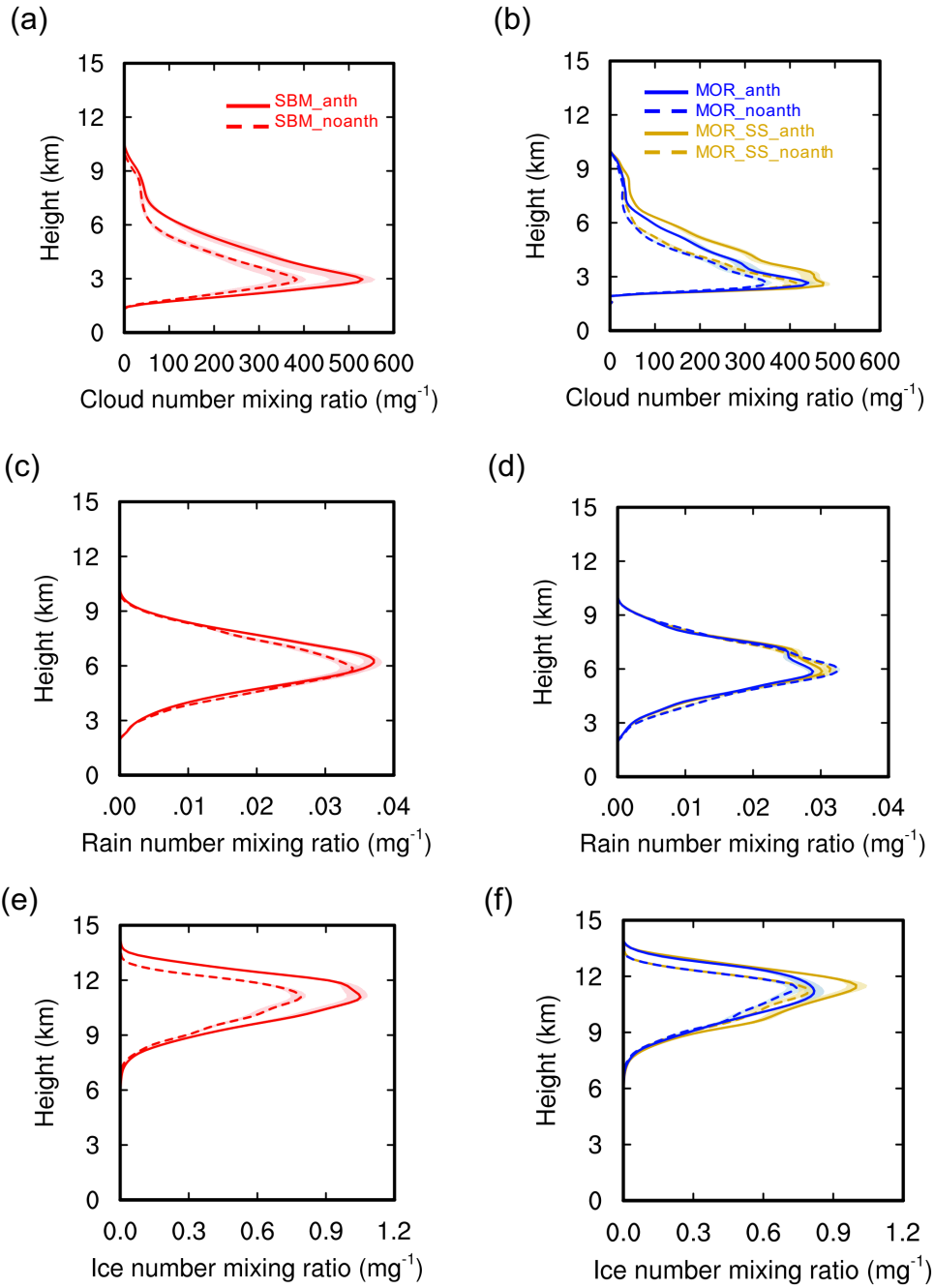
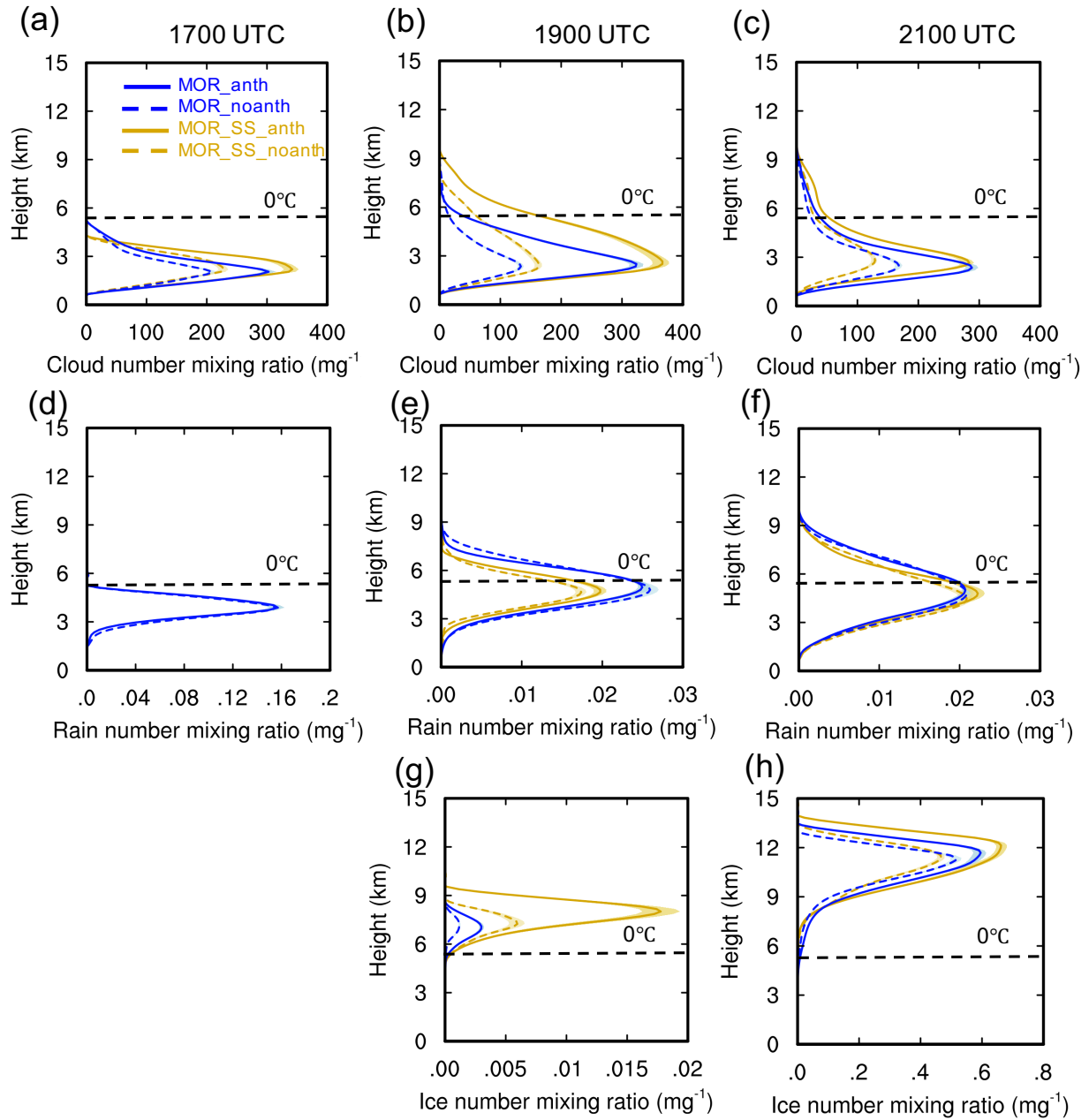851   **Figure 15** Same as Figure 14, but for hydrometeor number mixing ratio.
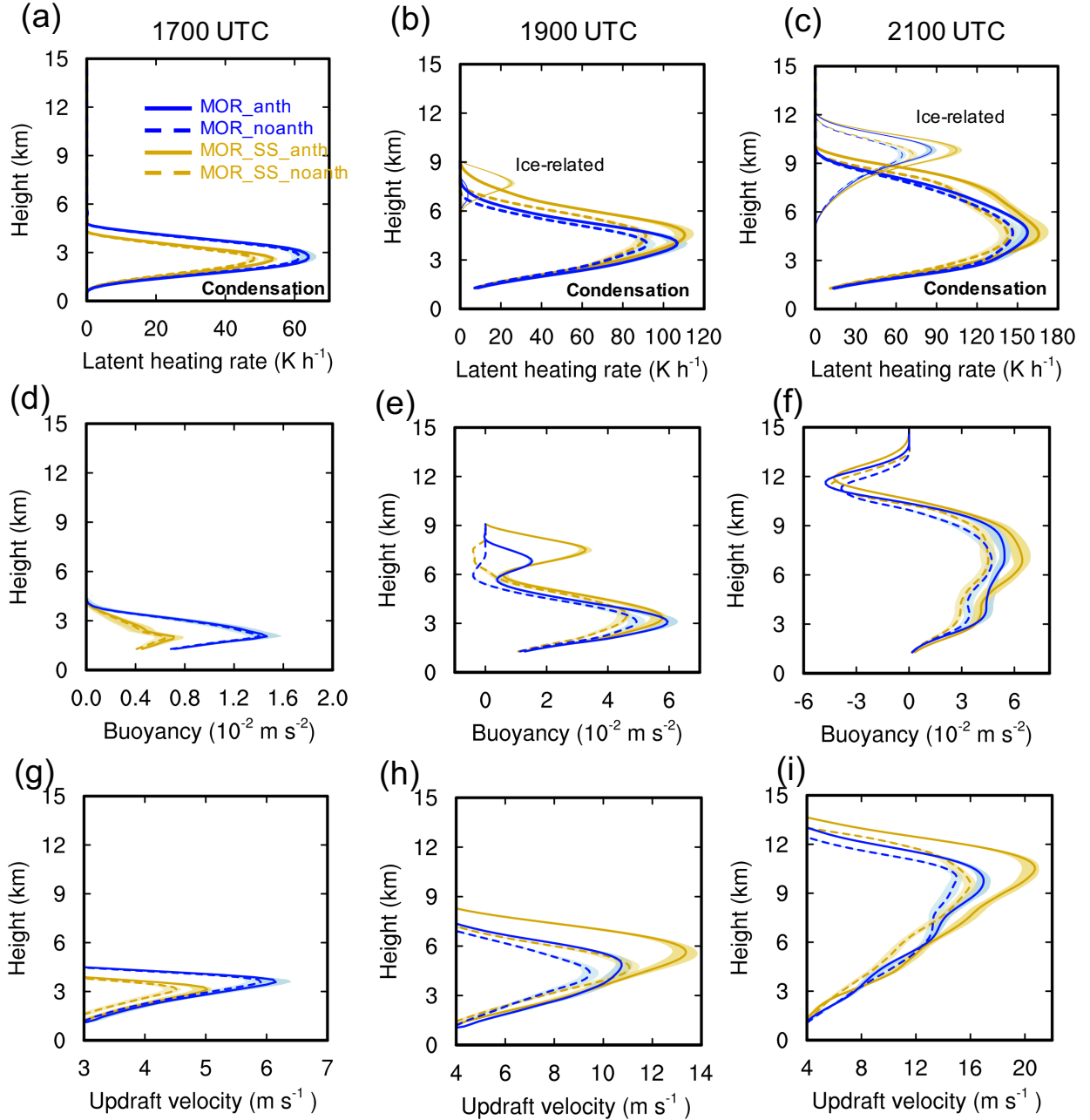
Figure 16 Vertical profiles of (a-c) latent heating rate from condensation (weighted lines) and ice-related processes (freezing, riming, and deposition; thin lines), (d-f) total buoyancy, (g-i) updraft velocity averaged over the top 25 percentiles (i.e., 75th to 100th) of the updrafts with value greater than 2 ms^{-1} from the simulations MOR_anth, MOR_noanth, MOR_SS_anth, and MOR_SS_noanth over the analysis domain as shown in the red box in Figure 7 at 1700 UTC, 1900 UTC and 2100 UTC. Data are processed in the same way as Figure 11.

Figure 17 Vertical profiles mass mixing ratios of (a-c) cloud droplet, (d-f) rain drop and (g-h) ice particle (including ice, snow, and graupel) averaged over cloudy points (hydrometeor mass larger than 10^{-5} kg kg^{-1}) from the simulations MOR_anth, MOR_noanth, MOR_SS_anth, and MOR_SS_noanth over the analysis domain as shown in the red box in Figure 7 at 1700 UTC, 1900 UTC and 2100 UTC. Data are processed in the same way as Figure 11.

Figure 18 Same as Figure 17, but for hydrometeor number mixing ratio.